applied sciences

Article

Semi-Automatic Image Processing System of Aeromagnetic Data for Structural and Mining Investigations (Case of Bou Azzer Inlier, Central Anti-Atlas, Morocco)

Ayoub Soulaimani [1,*], Saïd Chakiri [1], Saâd Soulaimani [1,2,*], Ahmed Manar [3], Zohra Bejjaji [1], Abdelhalim Miftah [4,5,*], Mohammed Amine Zerdeb [1], Yaacoub Zidane [1], Mustapha Boualoul [6] and Anselme Muzirafuti [7,*]

1 Geosciences Laboratory, Department of Geology, Faculty of Sciences, Ibn Tofaïl University, BP 133, Kénitra 14000, Morocco
2 Resources Valorization, Environment and Sustainable Development Research Team (RVESD), Department of Mines, Mines School of Rabat, Av Hadj Ahmed Cherkaoui, Agdal, BP 753, Rabat 10090, Morocco
3 Ministry of Energy Transition and Sustainable Development, Directorate of Geology, Agdal, BP 6208, Rabat 10090, Morocco
4 Research Team of Geology of the Mining and Energetics Resources, Faculty of Sciences and Technology, Hassan First University of Settat, BP 577, Settat 26000, Morocco
5 Laboratory of Intelligent Systems Georesources and Renewable Energies, Faculty of Science and Technology, Sidi Mohamed Ben Abdellah University, BP 2202, Fes 30000, Morocco
6 Laboratory of Geoengineering and Environment, Department of Geology, Faculty of Sciences, University of Moulay Ismail, Zitoune, BP 11201, Meknes 50000, Morocco
7 Dipartimento di Scienze Matematiche e Informatiche, Scienze Fisiche e Scienze Della Terra, Università Degli Studi di Messina, Via F. Stagno d'Alcontres, 31-98166 Messina, Italy
* Correspondence: ayoub.soulaimani@uit.ac.ma (A.S.); soulaimani@enim.ac.ma (S.S.); a.miftah@uhp.ac.ma (A.M.); anselme.muzirafuti@unime.it (A.M.)

check for updates

Citation: Soulaimani, A.; Chakiri, S.; Soulaimani, S.; Manar, A.; Bejjaji, Z.; Miftah, A.; Zerdeb, M.A.; Zidane, Y.; Boualoul, M.; Muzirafuti, A. Semi-Automatic Image Processing System of Aeromagnetic Data for Structural and Mining Investigations (Case of Bou Azzer Inlier, Central Anti-Atlas, Morocco). *Appl. Sci.* **2022**, *12*, 11270. https://doi.org/10.3390/app122111270

Academic Editor: Fabrizio Balsamo

Received: 3 October 2022
Accepted: 2 November 2022
Published: 7 November 2022

Abstract: Numerical analysis of geophysical data to uncover Precambrian belts and probably to enclose mineral deposits is becoming once more communal in mining activity. The method is founded on typifying zones branded to comprehend deposits and looking for analogous areas. The proposed work outlines a semi-automatic image processing system for the structural and mining investigation of the Bou Azzer inlier, which varies from preceding approaches as it is centered only on aeromagnetic data. The aeromagnetic signature of what seem to be geologically expressive features are pursued within the aeromagnetic items. Cobalt and associated mineralizations in the Bou Azzer inlier are recognized to arise nearby main crustal discontinuities revealing as significant shear zones, which turn act as drains for mineralizing fluids. Mineralization occurs in sectors of structural complexity beside the shear zones. Developing towards the semi-automatic uncovering of such regions, the furthermost prospective extents are those everywhere inferred structural complexity occurs next to the regions of magnetic discontinuity. The proposed method is mainly based on the approach developed by the center for exploration targeting. The study was led by means of aeromagnetic data from the Bou Azzer inlier, which is considered one of the most productive and prospective regions for minerals and base metal mineralization in Morocco. The combined results obtained from geological and geophysical data prove that prospective areas have a dominant trend of NNE-SSW, NW-SE, NNW-SSE, E-W, and NE-SW directions. The CET Grid and Porphyry Analyses show that the probable porphyry mineral deposit locations mainly concentrated in the center of inlier, the Foum Zguid dyke, and northern and eastern part, which correspond to the Bou Azzer ophiolitic complex and platform deposits of the Lower Neoproterozoic Tachdamt-Bleïda.

Keywords: geophysics; aeromagnetic survey; Bou Azzer inlier; structural and mining investigations; CET grid and porphyry analysis; Central Anti-Atlas; Morocco

1. Introduction

Located on the Anti-Atlas border, the Bou Azzer inlier includes two significant mines: the cobalt mine, which is close to Bou Azzer village, and the Bleïda mine, which produces copper and gold. It is thought to be one of Morocco's most productive and promising regions for minerals and base metal mineralization. Ground selection is an important step in mineral exploration. Exploration then takes place inside the boundaries of the preferred region once a license to do so is requested, known as a tenement, lease, or claim [1,2]. Raising to its potential, the Bou Azzer inlier was a subject of numerous surveys and research to explore the presence of other deposits and structural analysis, such as several studies elaborated by Miftah et al. [3,4], Bougouri et al. [5], Alvaro et al. [6], and Aabi et al. [7], or other studies based principally on simple data processing of geophysical data (magnetic, aeromagnetic, or gravity data) or on a geological approach, which had results with significant inaccuracies. In the framework herein, our study was led based on vast amounts of high-resolution aeromagnetic data acquired from the Moroccan Geology Department Ministry of Energy and Mines. The acquired data can be employed for geological mapping on a regional scale [8]. These data might be the sole way to assess the regional geology in geological terrains that have not been adequately exposed or examined [2,9].

We outline a semi-automated technique for effectively mapping geological contacts and favorable zones for mining prospection utilizing aeromagnetic data collected by a cesium magnetometer Scintrex Cs2 with a sensitivity of 0.01 nT. CET Grid Analysis employs advanced automated image analysis techniques and human data interaction to rapidly map geological structures (faults, joints, and fractures) and to determinate the mining potential of the study area. This method adds value to traditional data processing and provides consistent results that can be reproduced. The CET Porphyry Analysis was used to seek the magnetic response of an idealized porphyry mineralizing system within magnetic data sets. The method finds circular anomalies that are associated with the central intrusion and inner alteration zone [10].

This article outlines a current study on the semi-automatic assessment of a large aeromagnetic data set using advanced image processing techniques to detect favorable zones for mining exploration that present advantages compared to other simple (classical) processing approaches used by researchers such as Soulaimani et al. [11,12], Bouiflane et al. [13], and Mamouch et al. [14]. For big data assessments, the proposed semi-automatic approach has advantages and may result in lower exploration expenses and more accurate identification of the mineral resources [11,12] and reliable structural analysis. The desired study concept searches for promising districts using a broad geophysical data set that is based on a structural and geological model of the area [14], but does not necessitate in-depth understanding of the local geology [15]. Other quantitative prospective analysis methods deviate from this strategy by requiring a geological map of the region [16,17]. This method also differs from the aforementioned systems and other geophysics-based prospectivity analysis methods in that it does not require a thorough understanding of the patterns of known deposits that are then utilized as models for prediction [4]. The objectives of this study are to conduct a geophysical mapping of the Bou Azzer inlier to determine the mining potential and structural control on mineralization by combining geological and geophysical data. Thus, the results obtained will be able to guide the next prospecting campaigns in the region.

2. Materials and Methods

2.1. The Geological and Metallogenic Setting of the Study Area

2.1.1. Anti-Atlas Belt

The Anti-Atlas forms a vast anticlinal bombardment-oriented ENE-WSW between Ifni and Erfoud where the Precambrian basement outcrops in small inliers under a cover of the Late Neoproterozoic and Paleozoic. This bombardment of thermal origin, interpreted as being linked to the heightening of the lithosphere/asthenosphere limit (LVZ), is dated to the Neogene [18,19], and it is limited to the north by the tectonic lineament of the South Atlas accident and to the south and SSE by the Paleozoic basins of Tindouf and Bechar, called the

Saharan platform. These reliefs extend from the area of Bas-Drâa in the southwest to Tafilalt in the northeast. The Anti-Atlas is fragmented into several massifs: to the west the Anti-Atlas of Tafraout, to the east the ancient volcano of Jebel Siroua culminating at 3305 m, and even more to the east the Jebel Saghro beyond the Oued Drâa. The Precambrian outcrops in several inliers under the unconformity cover of the Paleozoic. From west to east, we can see the inliers of Bas-Drâa, Ifni, Kerdous, Igherm, Zenaga, Siroua, Bou Azzer, Saghro, and Ougnat. The morphology as well as the structure of these inliers change according to the nature of the rocks, and they are generally presented in the form of depression when they are formed of soft materials. When they are formed of hard materials, buttes witnesses appear. Marked by the absence of the Archean, the oldest terrains of the Anti-Atlas date back to the Paleoproterozoic. These inliers make it possible to reconstruct a segment of the Pan-African belt and its foreland on the northern periphery of the West African Craton (WAC) [20]. These last so-called inliers are separated by eroded corridors, commonly called the Feijas. They are essentially constituted by the different soft levels of the Paleozoic series, thus the cover. The Anti-Atlas is structured by two major faults: the South Atlas Fault in the north (SAF) and the Anti-Atlas Major Fault in the south (AAMF), crossing the chain transversely (Figure 1).

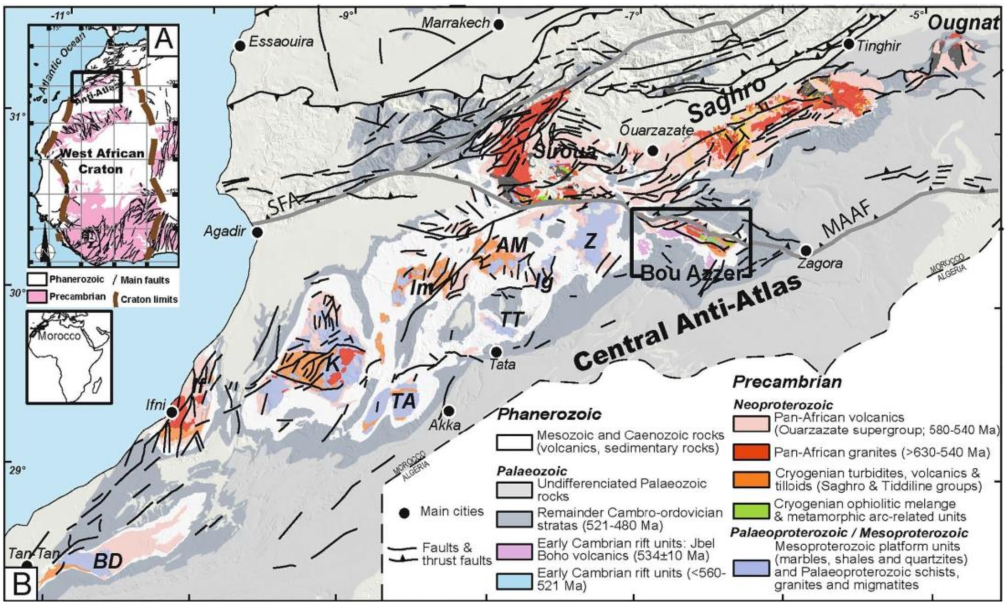

Figure 1. Localization of the studied area at (A) the West African Craton scale and (B) at the Moroccan Anti-Atlas scale [21].

2.1.2. The Bou Azzer–El Graara Inlier

Located in the central part of the Anti-Atlas, the Bou Azzer–El Graara inlier represents an important segment of the Anti-Atlas region for the perception of Pan-African events [20,22]. The Precambrian outcrops there in two contiguous massifs, Bou Azzer and El Graara, following a Variscan antiform structure which runs along the major accident of the Anti-Atlas [23]. This accident subdivides the Precambrian Anti-Atlas terrains into two distinct domains, a cratonic domain to the SW and a recent Pan-African domain to the NE. The Bou Azzer inlier is divided into eight lithological units (Figure 2) having undergone greenschist facies metamorphism linked to a deformation phase dated at 685 Ma [24,25], which in order of descending age are the following:

- Tachdamt–Bleïda Group (NP1-2): attributed to the Upper Tonian–Lower Cryogenian and consisting of sandstone-quartzites and siltstones and formed by platform deposits characterized by alkaline tholeites emplaced in a fissural context. Another group of calc-alkaline basalts generated in an arc and back arc context has been highlighted;

- Lower Cryogenian Tichibanine–Ben Lgrad Group (NP2i): consisting of siltstones enclosed in granitoids of the Taghouni massif as well as a mixture of volcano-sedimentary and volcanic series;
- Assif n'Bougmmane–Takroumt plutono-metamorphic complex: consisting of orthogneiss and paragneiss attributed to the Lower Cryogenian (NP2i). These rocks are crosscut by anatectic granitoids attributed to the Upper Cryogenian (NP2s);
- Bou Azzer–El Graara Group (ophiolitic complex): attached to the Upper Cryogenian (658 ± 9 Ma), comprising here serpentinized mantle peridotites, microgabbro–dolerite veins, basalts, and a volcano-sedimentary unit;
- Dioritic to granodioritic intrusions at the Cryogenian–Ediacaran boundary (NP2-3): including the Boufrokh and Bou Azzer massifs, as well as the polyphase Taghouni massif;
- Bou Lbarod–Iouraghene Group (NP3i): consisting of Lower Ediacaran ignimbrites and andesites dated at 625 ± 8 Ma;
- Tiddiline Group: attached to the Lower Ediacaran (NP3i, 606 ± 4 Ma, Alougoum map) and made up of sandstone and siltstone, with local rhyolite intercalations;
- Ouarzazate Group: attributed to Upper Ediacaran (NP3s, 566 ± 4 and 567 ± 5 Ma) and consisting essentially of ignimbritic pyroclastic flows of dacitic to rhyolitic composition associated with tuffs and pyroclastic breccias as well as sedimentary volcano-detrital deposits. Its summit is characterized by the appearance of andesitic flows interlayered with ignimbritic flows.

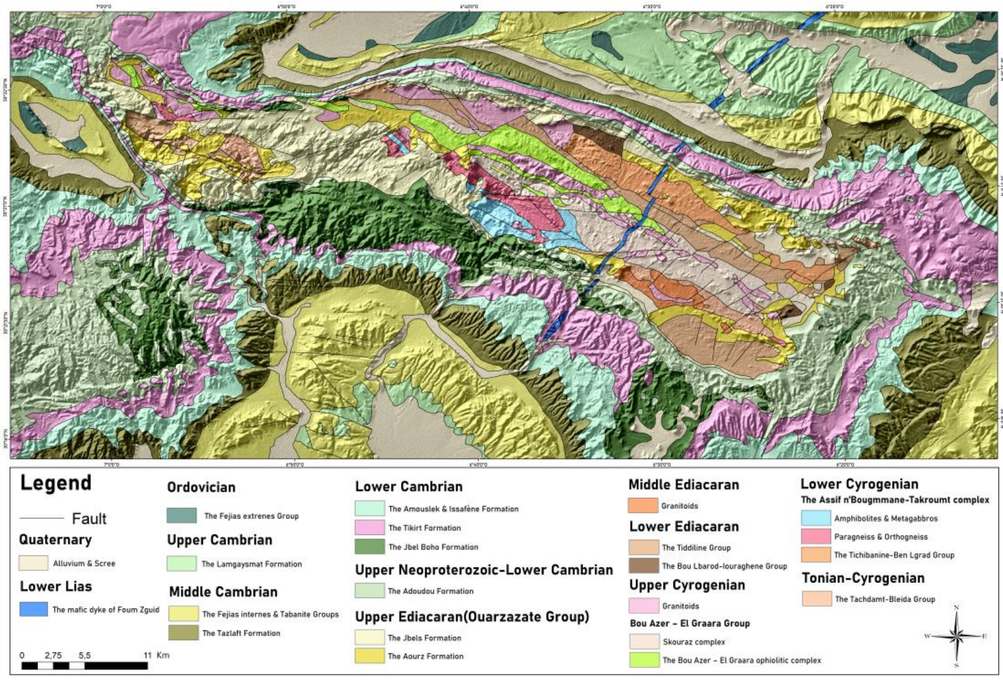

Figure 2. Geological setting of Bou Azzer inlier after 1/50,000 geological maps of Aït Ahmane and Alougoum modified after [26].

2.1.3. The Ophiolitic Complex of Bou Azzer

Described for the first time by Leblanc et al. [27–29], this ophiolitic unit consists of a strongly tectonized and dismembered ophiolitic assemblage outcropping in the center of the Bou Azzer inlier. It is composed of the following: serpentinized upper mantle peridotites (40% of the total complex); basic and ultrabasic cumulates (layered gabbros) (10–15%); large stocks of quartz diorites (10%); basic lavas with pillow lavas; and a volcano-sedimentary series. The studies of Hefferan et al. made it possible to obtain an approximate age of 762 Ma on plagiogranites [30]. El Hadi et al. [31] estimate the age of the formation of the Bou Azzer ophiolite at 697 Ma.

The mantle section of the Aït Ahmane sequence consists essentially of spinel harzburgites associated with rare dunitic lenses, both fully serpentinized [32]. The largest outcrop of serpentinite is located near the locality of Aït Ahman. The serpentinites (40% of the total complex) are derived from harzburgites and dunites showing a tectonic fabric. The Aït Ahmane serpentinites (Bou Azzer ophiolite, Morocco) are likely derived from ultra-refractory peridotites that have undergone extensive partial melting, as evidenced by the Cr-spinel chemistry core, supporting the supra-subduction zone origin advocated by previous research [33].

2.1.4. Bou Azzer Mining District

Located 120 km south of the city of Ouarzazate, the Bou Azzer mining district contains more than 100 cobalt arsenide orebodies (Figure 3). They are spatially and genetically associated with serpentinites, resulting from the transformation of ophiolitic ultrabasites. Their morphology largely depends on the rheology and the structuring of the surrounding rocks.

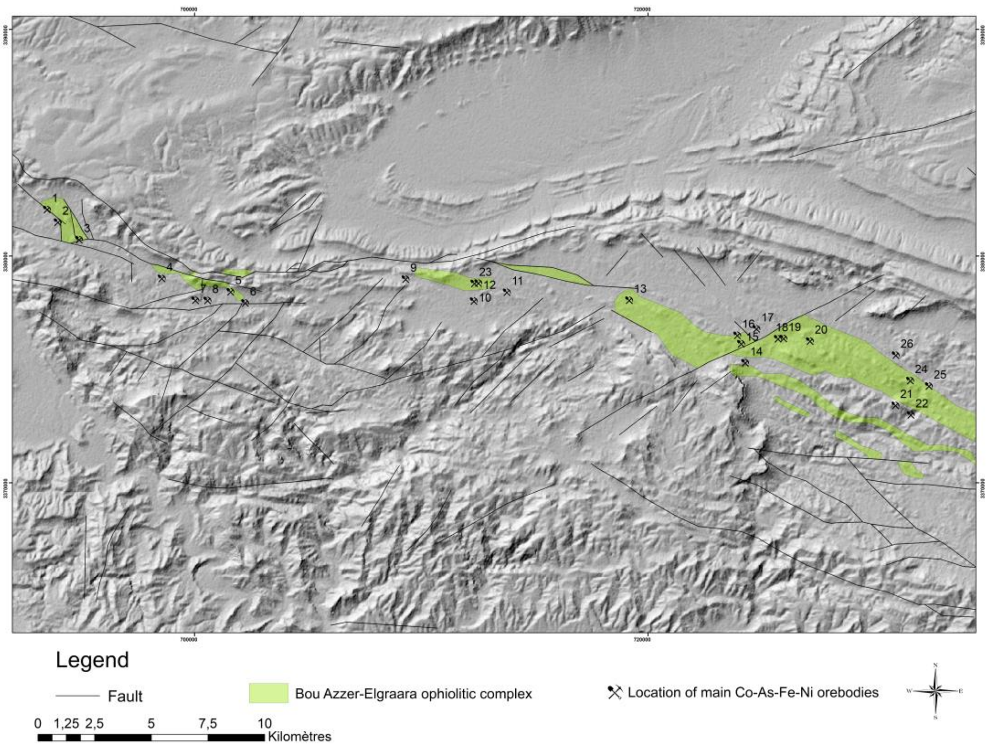

Figure 3. Localization of Bou Azzer–El Graara ophiolitic complex and the main Co-As-Fe-Ni orebodies: **1.** Méchoui, **2.** Khder, **3.** Nickeline vein, **4.** Taghouni, **5.** Bou Azzer Vein No. 2, **6.** Bou Azzer East deposit, **7.** Vein No. 5, **8.** Vein No. 7, **9.** Aghbar, **10.** Bouismas, **11.** Tamdrost, **12.** Oumlil, **13.** Ambed, **14**, **15**, **16.** Ightem, **17.** Inguijem, **18.** Agoudal Centre Quarry, **19.** Agoudal, **20.** Agoudal open pit, **21.** Vein No. 52, **22.** Vein No. 53, **23.** Vein No. 55, **24.** Vein No. 61, **25.** Aït Ahmane, **26.** Dolomite outcrop Aït Ahman.

Several ore models grouped into six types of orebodies (Figure 4) are distinguished [34]:

- The vein-type mineralization of filon 7/5 is located at the tectonic contact of the serpentinites with the quartz diorite; the mineralization is in the form of aligned ENE/WSW columns. This type is mainly controlled by major Pan-African faults.
- Tamdrost-type mineralization includes extension veins, cruisers, and bodies in the form of ore masses; the mineralization associated with these ore masses is particularly rich in nickel. The "Ambed carapace", a product of Late-Pan-African alteration of serpentinite, constitutes the main metallotect of this type of mineralization; it is represented by vein-type orebodies but also in filling of extensive fractures.

- The Méchoui type includes secondary veins, oriented NW and NE and included in the quartz diorite in contact with the serpentinites in the form of opened slits.
- Aït Ahmane type veins are solitary structures in the diabases and gabbros of the Bou Azzer ophiolitic complex. The disseminated texture predominates there, which makes their recovery more difficult.
- Aghbar-type mineralization is concentrated on the flanks of the diapir in relation to the synchronous fracturing of the mineralizing system. It is controlled by the diapiric rise (doming) of the serpentinites.
- Vein II type mineralization is located at the northern contact of the serpentinite massif. Its particularity lies in the presence of Pan-African basic rocks between the serpentinite and the Adoudounian cover, which explains the development of the mineralization in veins rather than in ore masses.

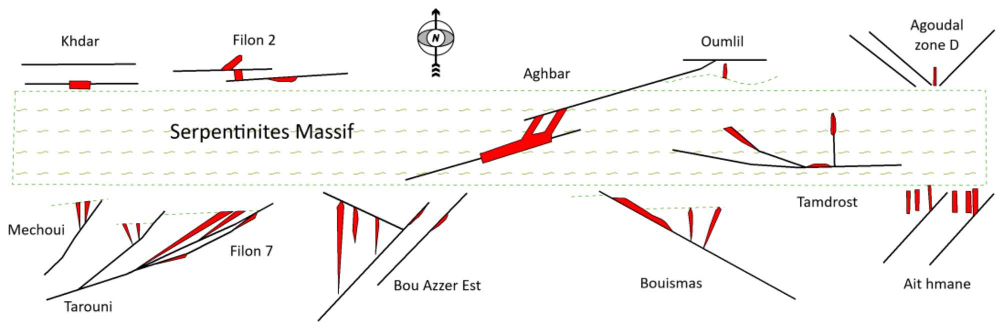

Figure 4. The Bou Azzer arsenide vein system modified after [35].

The paragenetic sequence of Bou Azzer mineralization has been frequently defined and discussed by various authors [21,29,34,36–39]; thus, four major primary paragenetic stages have been defined in Bou Azzer (Figure 5):

- Pre-arsenide "Stage 1": chalcopyrite, molybdenite, sphalerite, pyrite, amphibole, chlorite, sericite, brannerite, and hematite;
- Arsenide, Fe-arsenide, and Sulpharsenide "Stage 2": arsenopyrite, skutterudite, magnesium-brannerite, talc, loellingite, Co arsenides, cobaltite, gold, Ni, and Fe arsenides;
- Sulfide, sulfosalt, and native element "Stages 3 and 4": molybdenite, chalcopyrite, bornite, pyrite, sphalerite, galena, Au, Ag, and Bi.

Various studies by different dating methods have been carried out to determine the age of the Bou Azzer deposits, but the latter is still debated. Leblanc et al. estimates an emplacement of mineralization in the Precambrian and more precisely in the Neoproterozoic [29]. Ennaciri et al. [39] calculated it an age of 550 Ma in a brannerite related to the Co mineralization of the "Cruisers".

Levresse el al. [40] determined an age of Ar/Ar muscovite at 392 $\pm$ 15 Ma and an adular age at 218 $\pm$ 8 Ma, respectively, in the "Cruisers" of the Tamdrost and Filon 7/5 mining site. Co veins intersecting trachyte sills have been dated in U/Pb on zircon at 533 $\pm$ 2 Ma. Gervilla el al. [41] obtained U/Pb ages on brannerite in Vein 7/5 between 385 and 375 Ma, and linked these ages to precollision tectonics of the Hercynian orogeny.

The Bou Azzer genetic model is still the subject of great debate concerning both the absolute age of the mineralization and the determination of the source(s) of metals and arsenic. A conventional genetic model stipulated that the origin of cobalt is in serpentinite, magnetite, and certain levels rich in sulfides, with a first deposit of sedimentary cobalt in channels related to the Ambed carapace, reconcentrated by later tectonic phases and more particularly in the Hercynian [29]. Maacha el al. [42] give the entire mineralization a Late-Pan-African age and propose a model that combines the interaction between exogenous chloride-laden fluids and endogenous As, Mo, and Se-bearing fluids [42–45]. The model was confirmed by Ghorfi el al. [46]. The same model was taken up by Maacha el al. [35], which explains that a polyphase metallogenic system whose ultimate stage corresponds to a mixture between the exogenous fluids loaded with chlorides and cobalt, Ni and As leached from the serpentines (Figure 6), and with a volcanogenic fluid carrying selenium, molybdenum, bismuth, and gold is the source of economic mineralization [35,46,47]. Major accidents inherited in the Pan-African orogeny served as conduits for mineralizing fluids [21].

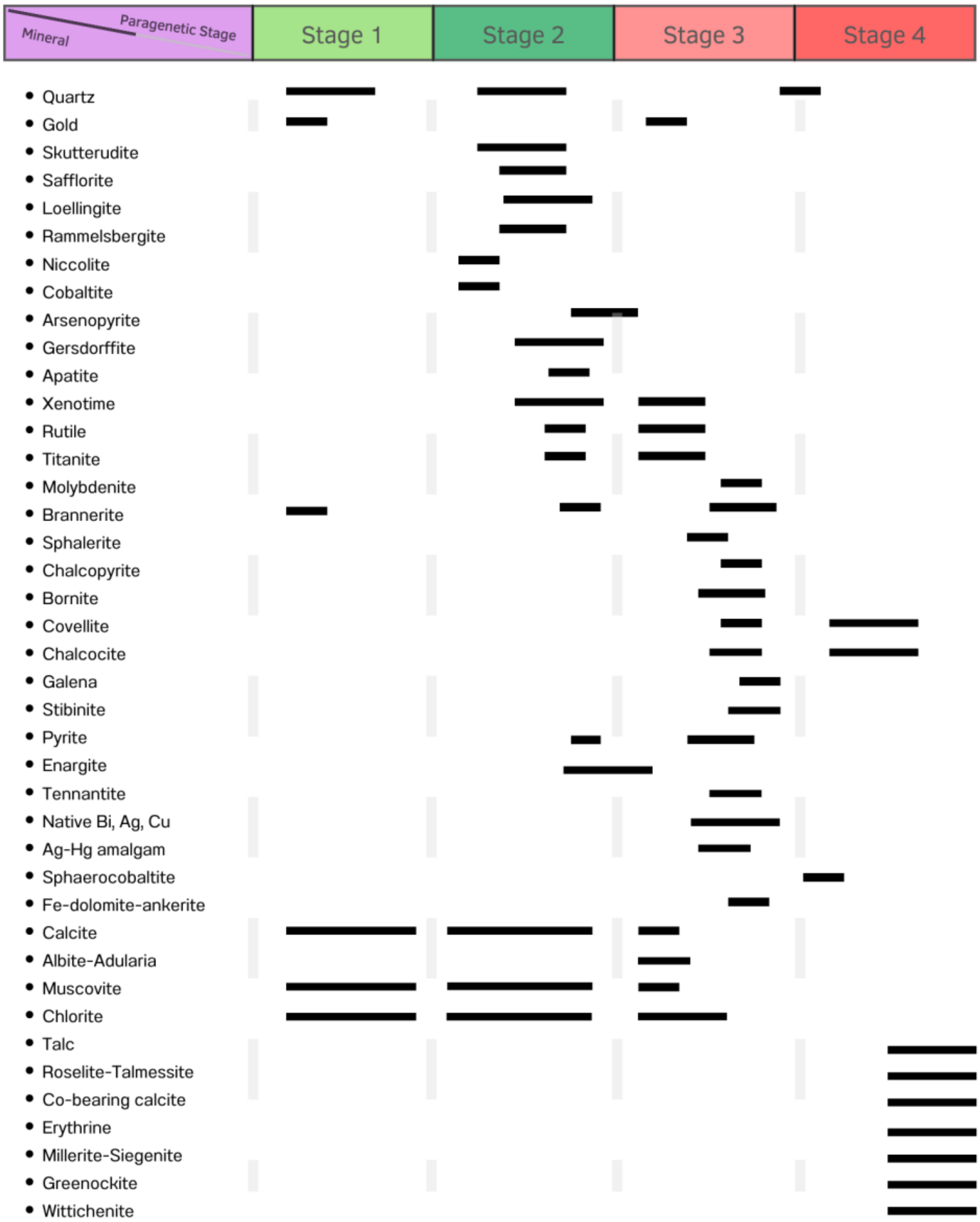

Figure 5. Polymetallic Bou Azzer district paragenetic sequence modified from [48].

2.1.5. Bleïda Mining District

Located in the SE part of the Bou Azzer inlier (Figure 7), the copper deposit of Bleïda has recovered much from the mining fame of the Bou Azzer–El Graara inlier.

Bleïda copper mineralization is hosted in platform deposits of the Lower Neoproterozoic Tachdamt–Bleïda Group, which is part of the Taghdout–Lkest Group defined on the northern margin of the West African Craton [5,49]. This series takes the form of an elongated strip WNW-ESE over about 11 km with an average width of 2 km. The age of this platforms series has been established at 788 ± 9 Ma [50]. It constitutes the oldest unit of the inlier; the Bleïda district is located at the eastern end of the Bleïda granodiorite, dated to 579.4 ± 1.2 Ma [51]. Two zones are distinguished (Figures 8 and 9), with two different types of mineralization [52]. The northern zone located in several levels of the Bleïda series: in the pelites (ore masses 60), at the contact between the pelites, and the schist-sandstone series (ore masses 113, 112, 110, 107, 106, and 125), or in the schist-sandstone unit (ore masses of Bleïda west). It contains the richest mineralization with an average Cu content of 9.34% for a tonnage of 1,800,000 t. The mineralization of Bleïda is predominantly copper and iron sulfides expressed in the form of bornite, chalcopyrite, and pyrite, which draw a zonality common to all the ore masses and around the ENE-WSW faults and their NE and NS satellites (Figures 8 and 9).

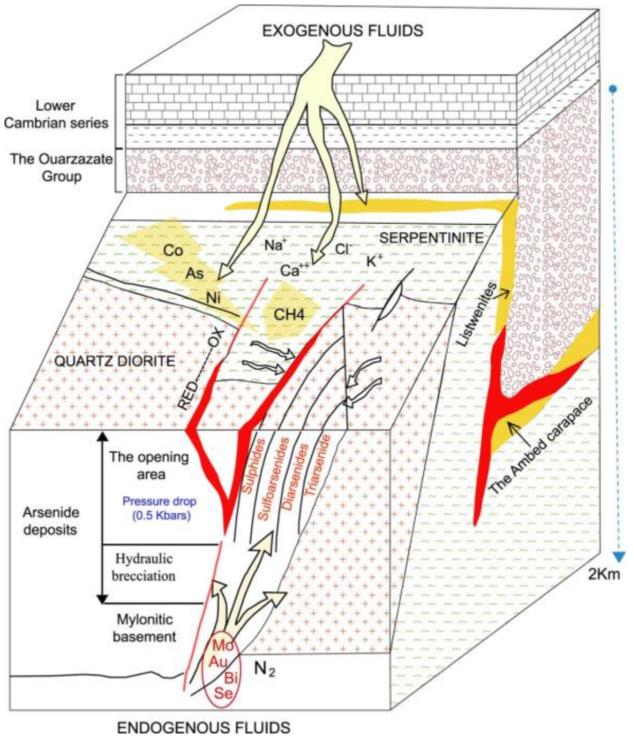

Figure 6. Proposed genetic model of the Bou Azzer Co–Ni deposits modified by [47] after [35].

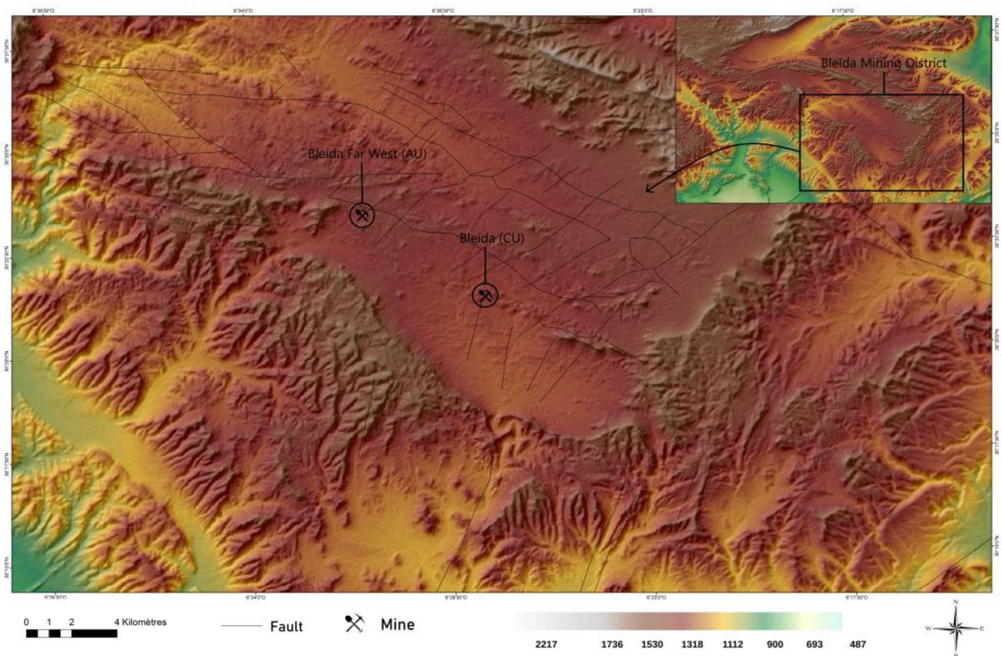

Figure 7. Location of the Bleïda mining district on the DEM of the Bou Azzer–El Graara inlier.

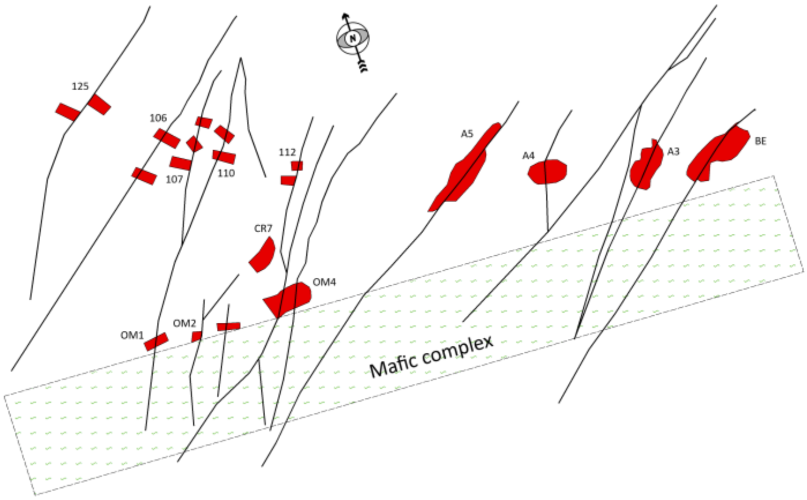

Figure 8. The pattern of fracturing that controls Bleïda sulfide bodies modified after [53].

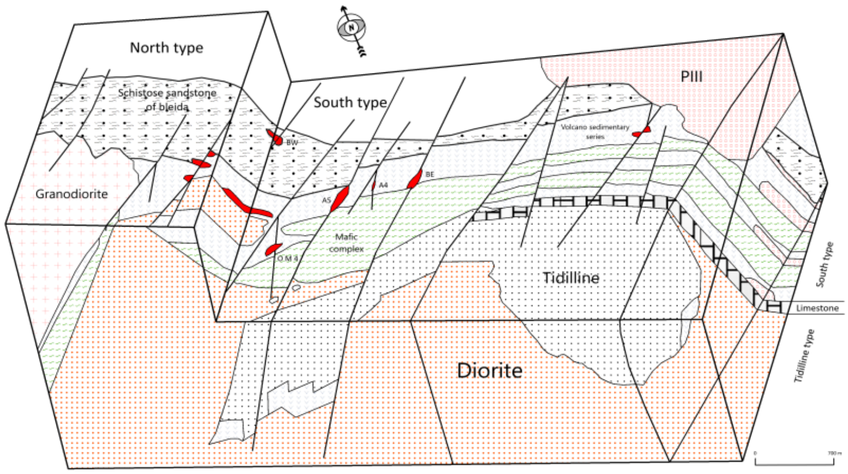

Figure 9. Schematic diagram explaining the structural character of the copper mineralization system at Bleïda modified after [53].

With regard to the formation mode of the Bleïda deposit according to [27–29], the primary mineralization of Bleïda is dispersed in the shales, and is remobilized and reconcentrated under the influence of the intrusion of the Bleïda granodiorite; they emphasized the stratiform aspect of the mineralization within the volcano-sedimentary host. In this context, the Bleïda stratiform copper deposit is interpreted as a sulfide mass emplaced prior to the Pan-African compressions [27–29]. For Mouttaqi el al., the copper mineralization of Bleïda is of the SEDEX type, set up in an extensive context with strong exhalative activity [53,54]. This hypothesis is based on the importance of hydrothermal facies intercalated at different levels of the Bleïda series (jasper, banded iron, chloritites, etc.).

2.2. Methodology

2.2.1. Aeromagnetic Data Set

Geophysics is utilized frequently in mining exploration [55], geological analysis, and structural analysis. It is a crucial component of the majority of mining exploration projects. Additionally, it is extensively employed because it can swiftly and cheaply map broad areas, highlight minor physical differences in geology that the geological field could not otherwise notice, and find the presence of a variety of exploitable deposits [3,56].

The Australian company Géoterrex-Dighem acquired the used data in 1998 and 1999 on behalf of the Ministry of Energy and Mines. A Eurocopter AS35OB2 and AS35OB3 helicopter with video recording equipment was used to collect data (video camera PAL). The

500 m diameter flight lines were spaced at an angle of N15° to N315° [57]. The observations were made using a cesium magnetometer with a sensitivity of 0.01 nT and an average ground clearance of 30 m. In the initial data processing, evident noisy data were removed, closing errors were identified, and diurnal changes were eliminated [4]. A residual magnetic anomaly data set was created by subtracting the International Geomagnetic Reference Field (IGRF) of 1999 from the total field magnetic data that were rectified.

The residual magnetic anomaly map was digitized at a 250 m grid interval because the original digital data were not available, and the digitized data were then gridded at a 100 m interval to create a digital residual magnetic anomaly (RMA) data set. By lowering the residual magnetic anomaly (RMA) data to the north magnetic pole [58], a reduction to the pole (RTP) magnetic anomaly data set was created, which eliminated the bipolar impact of the Earth's magnetic field. RMA and RTP magnetic anomaly maps were then created using color images of the RMA and RTP grids [57].

2.2.2. Data Analysis

To investigate the aeromagnetic data which were created by digitizing a set of eight regional aeromagnetic maps, a database was created including the residual field, which was used to save processing results, using the Geosoft Oasis montaj RTP filter to reduce the pole (RTP) of the residual magnetic field with the following inputs: the inclination, the declination in 1999 of the magnetic field, and residual grid file. The output is the residual grid file reduced to the north magnetic pole.

Therefore, the pole reduction was carried out with an inclination of 41.5° N and a declination of 4° W in order to place the anomalies precisely above the relevant geological bodies and to lessen the impact of magnetic changes brought on by the dipole magnetic field [59]. Recall that Baranov et al. [60] and Baranov and Naudy [61] proposed a mathematical strategy known as pole reduction, which is calculated in the frequency domain [60,61] using the filter operator [62], to simplify the magnetic anomaly. We employed the minimal curvature gridding approach for data interpolation [63].

The Geosoft Oasis montaj CET Grid Analysis and CET Porphyry Detection Extensions were used to implement a semi-automatic image processing system for grid analysis and porphyry analysis. Tools for automated lineament detection of gridded data are included in CET Grid Analysis, together with tools for texture analysis, phase analysis, and structure discovery (Figure 10). These are flexible algorithms that can be used for threshold detection, lineament detection, edge detection, and grid texture analysis [64–67], while CET Porphyry Detection was created specifically to find the magnetic signals of porphyry. A roughly round center intrusion is surrounded by concentric, almost circular alteration zones that are indicative of hydrothermal alteration associated with porphyry-style mineralization [64–67].

2.3. Grid Analysis

2.3.1. Texture Analysis

a. Standard Deviation

The standard deviation of the data values is determined within the immediate neighborhood [68] and offers an approximation of the local variation in the data. Significant features frequently show significant variation from the baseline signal. The standard deviation of the cell values xi for N cells with a mean value of is given by the following:

$$\sigma = \sqrt{\frac{1}{N}\sum_{i=1}^{n}(X_i - \mu)^2} \tag{1}$$

b. Entropy

The entropy operator [9] provides a measure of the textural information within localized windows (or *neighborhoods*) in a data set. It measures the statistical randomness of neighborhood data values by first quantizing the data into discrete bins and then analyzing the total number of distinct values resulting from that quantization. Given a specified number of bins, n, for each cell i in a $k \times k$ sized neighborhood, form a histogram and compute the entropy as follows:

$$E = -\sum_{i=1}^{n} P_i \log(P_i) \tag{2}$$

where the probability p is obtained after normalizing the histogram of n bins.

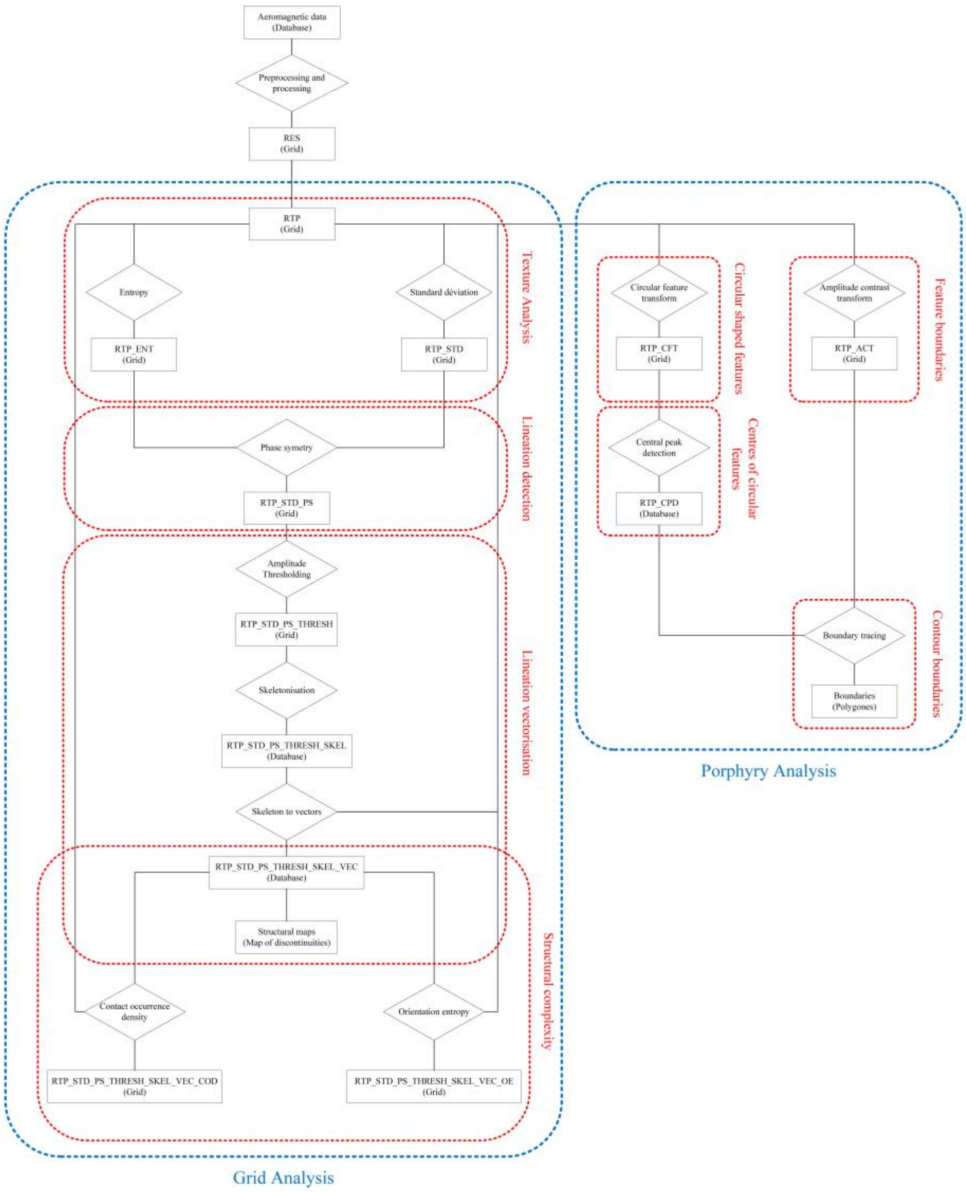

Figure 10. Flowchart of the processing method.

2.3.2. Lineation Detection

a. Phase Symmetry

The phase symmetry algorithm [68–70] considers a line to be symmetrical across the line, e.g., perpendicular to the line. By locating axes of symmetry, this attribute helps in the detection of line-like patterns. It is also well known that a signal's symmetry and the periodicity of its spatial frequency are tightly related. As a result, it makes sense to use a frequency-based method to find axes of symmetry.

b. Phase Congruency

The limits of the majority of magnetic and gravitational anomalies are not clearly defined step edges but rather slowly moving bands, whereas standard gradient-based edge detection approaches find step edges. The phase congruency transform is a contrast-invariant edge detection technique based on detecting the local spatial frequencies, much like the phase symmetry transform [64]. It takes advantage of the fact that edge features appear when the local frequency components are most in phase with one another [70]. This finding can be compared to symmetry points where components are at extremes.

c. Amplitude Thresholding

Applying non-maximal suppression (NMS) to data in conjunction with amplitude thresholding is helpful for identifying ridges, since low values are suppressed while points of local maxima are kept [71]. Our NMS solution considers the local feature orientation to maximize feature continuity, which can be used to reduce noise and emphasize linear features [64].

d. Skeletonization

The skeletonization algorithm [72] is a morphological operation that takes a binary grid and skeletonizes each foreground object by iteratively eroding away its boundary cells until the object is only 1 cell wide.

2.3.3. Lineation Vectorization

a. Amplitude Thresholding

The contact occurrence density approach generates a heat map that highlights the high density of structural contacts [73], which include junctions and intersections of different structures and locations where structures have significant orientation changes.

b. Orientation Entropy

The orientation entropy operator [17] draws attention to places where structures can be found in a variety of orientations, highlighting potential structurally complex regions [2].

The following operator determines the statistical randomness of the orientations of all line segments inside a local window given an input of vectorized structures [1]:

$$E = -\sum_{i=1}^{n} P_i \log(P_i) \tag{3}$$

where the probability p is obtained after the normalizing the histogram of n bins.

2.4. Porphyry Analysis

2.4.1. Circular Feature Transform

The radial symmetry transform, which is used to calculate the circular feature transform (CFT), is intended to find circular-shaped features [74]. By determining where picture gradients converge or diverge, the transform emphasizes the centers of raised or depressed circular structures. The CFT allows for the specification of parameters that describe the radial size, circularity, and completeness of features of interest.

2.4.2. Central Peak Detection

The central peak detection [64] locates the middles of rounded structures from a circular feature transform (CFT). This is achieved by suppressing non-maximum circularity responses within each neighborhood in the data while preserving the maximum value. Thresholding is then applied so that only significant feature centers are retained.

2.4.3. Amplitude Contrast Transform

The amplitude contrast transform [13,75] measures the magnetic amplitude contrast of circular features at specific distances from their surroundings to highlight the feature boundaries. A circular feature in the magnetic contrast transform output will appear as a "halo", which coincides with the circular rim of the feature. The algorithm used for the amplitude contrast transform is an extension of the radial symmetry algorithm used in the circular feature transform (Geosoft Oasis montaj).

2.4.4. Boundary Tracing

The boundary tracing process traces feature boundaries using an active contour algorithm [76]. Active contours (snakes) are splines that are iteratively drawn to the feature boundaries using an energy minimizing technique. The spline energy is a function (over s control points of the spline) of two internal constraints that control the shape of the spline, namely the elasticity and curvature, and one image constraint that specifies feature boundaries that are being sought.

$$E = \int (w_1 E_{cont} + w_2 E_{curv} + w_3 E_{image}).ds \tag{4}$$

The control weights w_1, w_2 and w_3 determine the bias in the contour characteristics. A heavy bias towards continuity will result in contour points that are evenly spaced.

2.5. Euler Deconvolution

When used on magnetic data, the Euler deconvolution method permits the establishment of magnetic sources. A quick and accurate assessment of the position, depth, direction, and dip of magnetic contacts is produced by the procedure [4]. The structural index of zero, which has been used to solve the Euler deconvolution problem, refers to contacts or lineaments [77,78]. It is necessary for the window size to be sufficiently large to account for major field and gradient variations while being consistently small enough to exclude the effects of many sources [79–81].

2.6. Analytic Signal

By centering anomalies over the magnetic body and having peaks at the borders of wide bodies [13], the analytic signal transform simplifies the magnetic signal of anomalies [82]. As a result, a straightforward relationship between the converted data and the magnetic bodies' geometry is seen. Analytic signal transform, in contrast to RTP, combines derivative calculations to provide an attribute that is independent of the inclination and magnetization direction of the Earth's main field [83–86].

3. Results and Discussion

3.1. Geological Fault Density Map

To identify fault trends, their trends were compared with mineralization zones. Furthermore, the fault density map (Figure 11) was prepared, which shows the association of mineralized faults. The dominant veins are with 45–60 degree azimuth, which are in very good agreement with the NE-SW faults. We also marked the presence of a second family of faults trending ENE-WSW, which represents the major Pan-African faults. Most of the faults have a NE-SW trend in the area with intense intersection of thrust and normal faults. The overlap between the faults map and the mineralized veins shows an intimate association between the ore veins and the fault zones. The fault density map corroborates with the field results, as it shows a high concentration of mineralization in areas with high fault density, which proves that these faults served as a drainage channel for hydrothermal fluid from the deep zones towards the subsurface.

3.2. RTP

When the magnetic RTP map was examined (Figure 12), a number of intersecting linear and circular structures with NNW-SSE drift and variable amplitudes were discovered. These features are related to dykes, faults, shear zones, and geological formations. We see a string of positive and negative anomalies located in the inlier's south central, western, and eastern regions. Additionally, we highlight significant positive anomalies with WNW-ESE trend mostly associated with the Bou Azzer inlier ophiolitic complex and a NE-SW trend primarily associated with the Foum Zguid dyke.

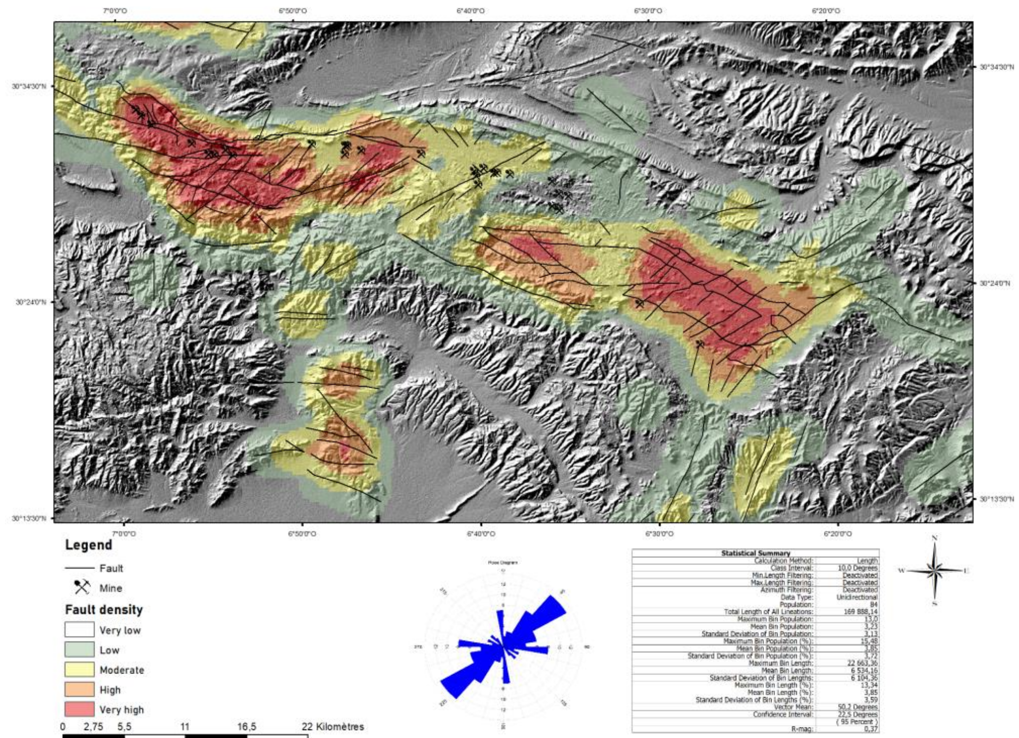

Figure 11. Geological fault density map of Bou Azzer inlier.

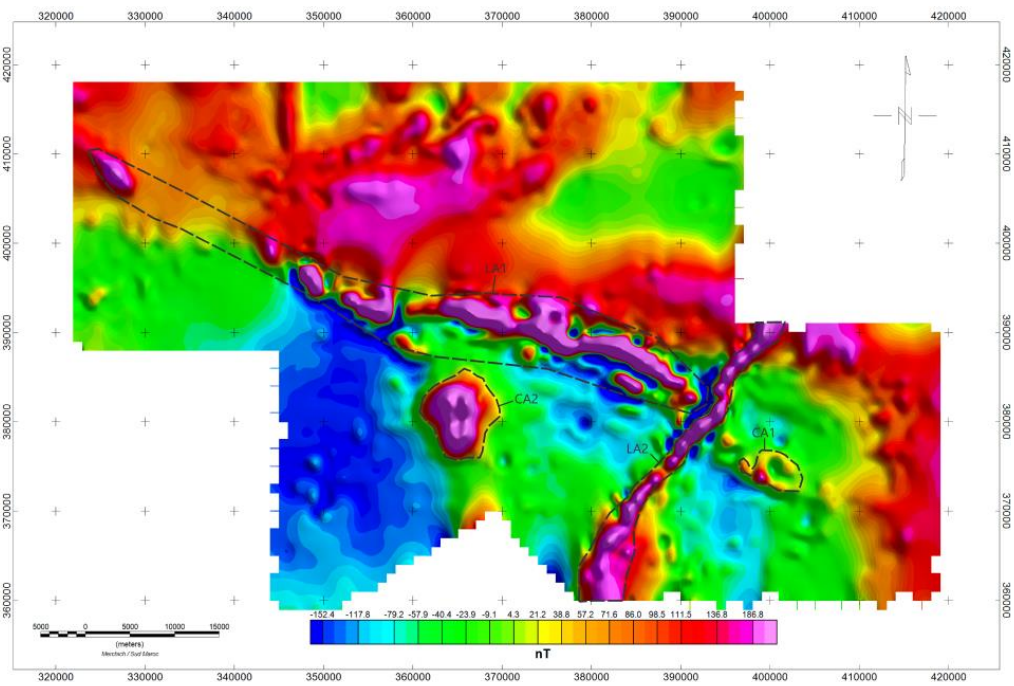

Figure 12. Residual magnetic anomaly map of Bou Azzer inlier and adjacent regions reduced to the magnetic pole.

The interactions between the disclosed rock components and the negative and positive anomalies are complete, and these interactions can be used to identify possible mineralization zones. Basanites, trachyandesites, trachyte, and rhyolites that are intruded by a syenitic pluton are revealed as geologic objects (Figures 2 and 12) by the processed aeromagnetic survey (RTP). The lack of linkage is particularly noticeable in the extent's southwest, where a strong negative anomaly is related to sedimentary overburden. Additionally, the majority of the WNW-ESE lineaments seen on the RTP map were absent on the geology map. The most significant relationship between the magnetic and geological framework can be summed up as follows:

1. Linear magnetic anomaly (LA1): runs along the inlier central part, corresponds to the ophiolitic complex of the Bou Azzer inlier with a WNW-ESE trend, and presents continuity towards to the west part, which can be considered as prospective areas for mineralization;
2. Linear magnetic anomaly (LA2): corresponds to the Foum Zguid dyke with a NE-SW trend, predominantly constituted by dolerite which matches to the high magnetic susceptibility;
3. Circular anomaly (CA1): corresponds to the Bleïda copper deposit located at the south-eastern part of the inlier;
4. Circular anomaly (CA2): located at the southern part of the ophiolitic complex, the anomaly corresponds to the alkaline complex of Jbel Boho formed mainly by basanites, trachyandesites, trachyte, and rhyolites that are intruded by a syenitic pluton.

3.3. Texture Analysis

The phase symmetry results achieved from standard deviation of the magnetic RTP (RTP) (Figure 13A) were from the aeromagnetic survey. It illuminates the local structure, which allows detecting the ridges as well as valleys. Symmetry detection (RTP_STD_PS) (Figure 13B) classifies the parts of magnetic discontinuity such as lithological boundaries, faults, and dykes (positive and negative features), as well as thresholder (RTP_STD_PS_THRESH) and skeletonized (RTP_STD_PS_THRESH_SKEL) structures. The skeletal structures are investigated to crop a set of straight-line segments that will be fitted and computed. Figure 14A,B exemplify the structure contact density heat map (RTP_STD_PS_TRESH_SKEL_VEC_COD) and the orientation entropy map (RTP_STD_PS_TRESH_SKEL_VEC_OE) created by a set of intersections that include crossings, junctions, and corners of the spotted line segments [73]. The high prospective areas can be identified as the intercepted or deviated linear structure. The line segments are used to calculate the contact occurrence density (Figure 14A) and orientation entropy (Figure 14B).

The lineaments which were extracted from the aborded approach presented in Figure 13A using the CET Grid Analysis tool of Geosoft Oasis Montaj are presented as extracted magnetic lineament overlaid on a standard deviation RTP map of the Bou Azzer inlier (Figure 13A). The rose diagram (Figure 15) of the obtained linear structures presents a dominant trend in the ENE-WSW direction, which agrees with previous work of [5,13,87–90]. A less dense but significant lineament trend occurs in many directions with a region extending from 1 to 50 Km. The obtained results and inspection with magnetic RTP and geological map are summarized below:

1. A good correlation between geological and magnetic structures was observed;
2. Contact between serpentine rocks and surrounding rocks could be considered as a prospective area for cobalt or associated mineralization;
3. The alignments of prospective areas had a dominant trend of NNE-SSW, NW-SE, NNW-SSE, E-W, and NE-SW directions;
4. The most prospective parts for cobalt, copper, and associated mineralizations are located on the zones with the high contact occurrence density and high orientation entropy in the Bou Azzer inlier and its surroundings.

3.4. Porphyry Analysis

The CET Porphyry analysis for the delineation of porphyry mineral deposits across the study area carried out at continuation distances from 300 m to 2100 m, which reflects the geology of the area (Figure 16A,B), identified fifty likely porphyry mineral deposit locations [64] mostly occurring within the Bou Azzer ophiolite complex [91], which become very visible when the generated porphyry mineral deposit is overlaid on the analytic signal map and circular feature transform map [92] (Figure 17A).

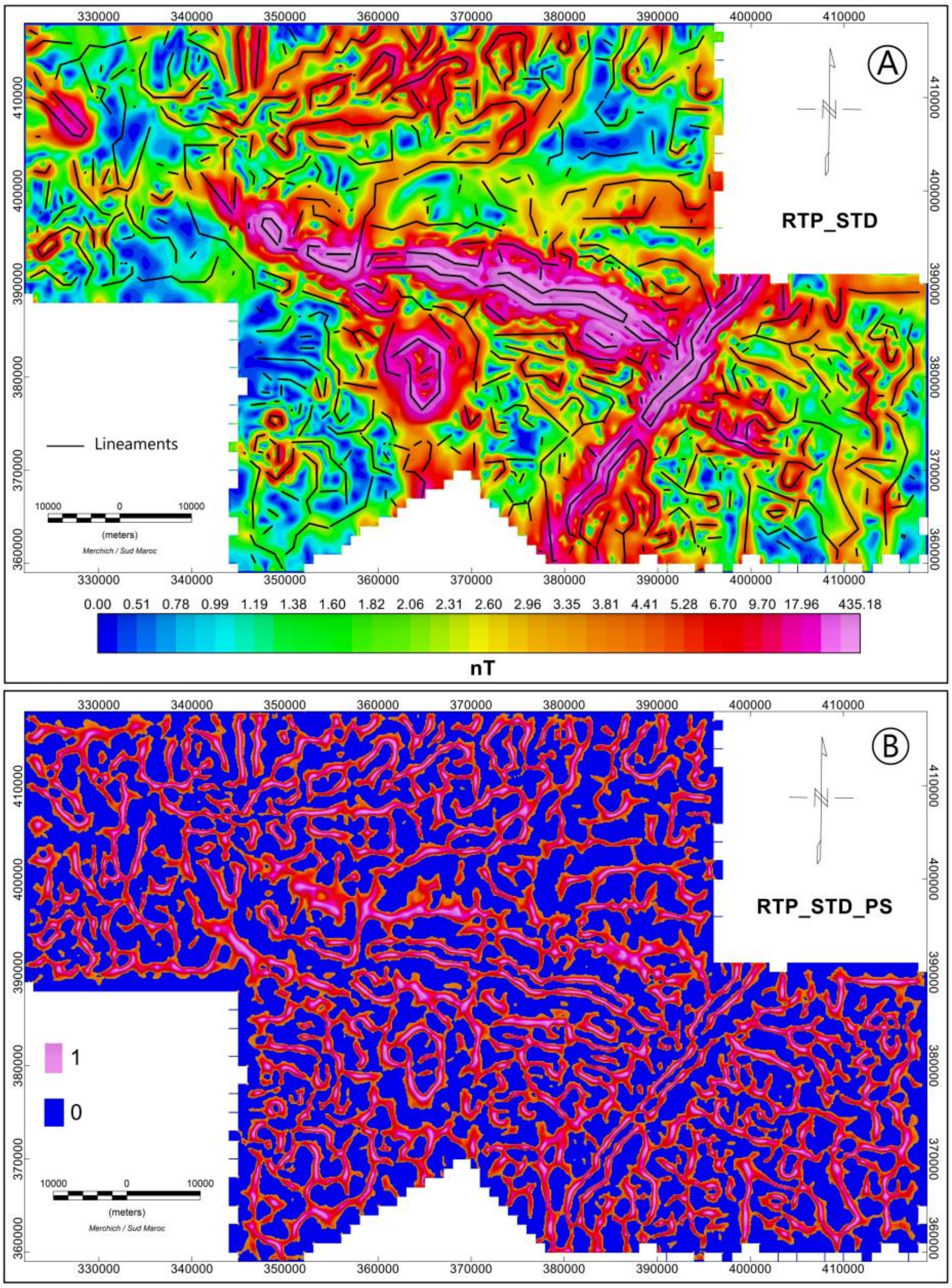

Figure 13. (**A**) Standard deviation of the RTP with the final obtained contacts and faults. (**B**) Thresholded amplitude of RTP_STD.

The delineated probable porphyry mineral deposit [93] locations mainly concentrated in the central part of inlier, in the Foum Zguid dyke [94,95], and in northern and eastern part (Figures 16B and 17A). The Bou Azzer cobalt deposit and Bleïda cooper deposit [6,96] were identified and occurred within the Bou Azzer ophiolitic complex and platform deposits of the Lower Neoproterozoic Tachdamt-Bleïda (Figures 16B and 17A). Fewer likely porphyry deposits were also identified around existent deposits.

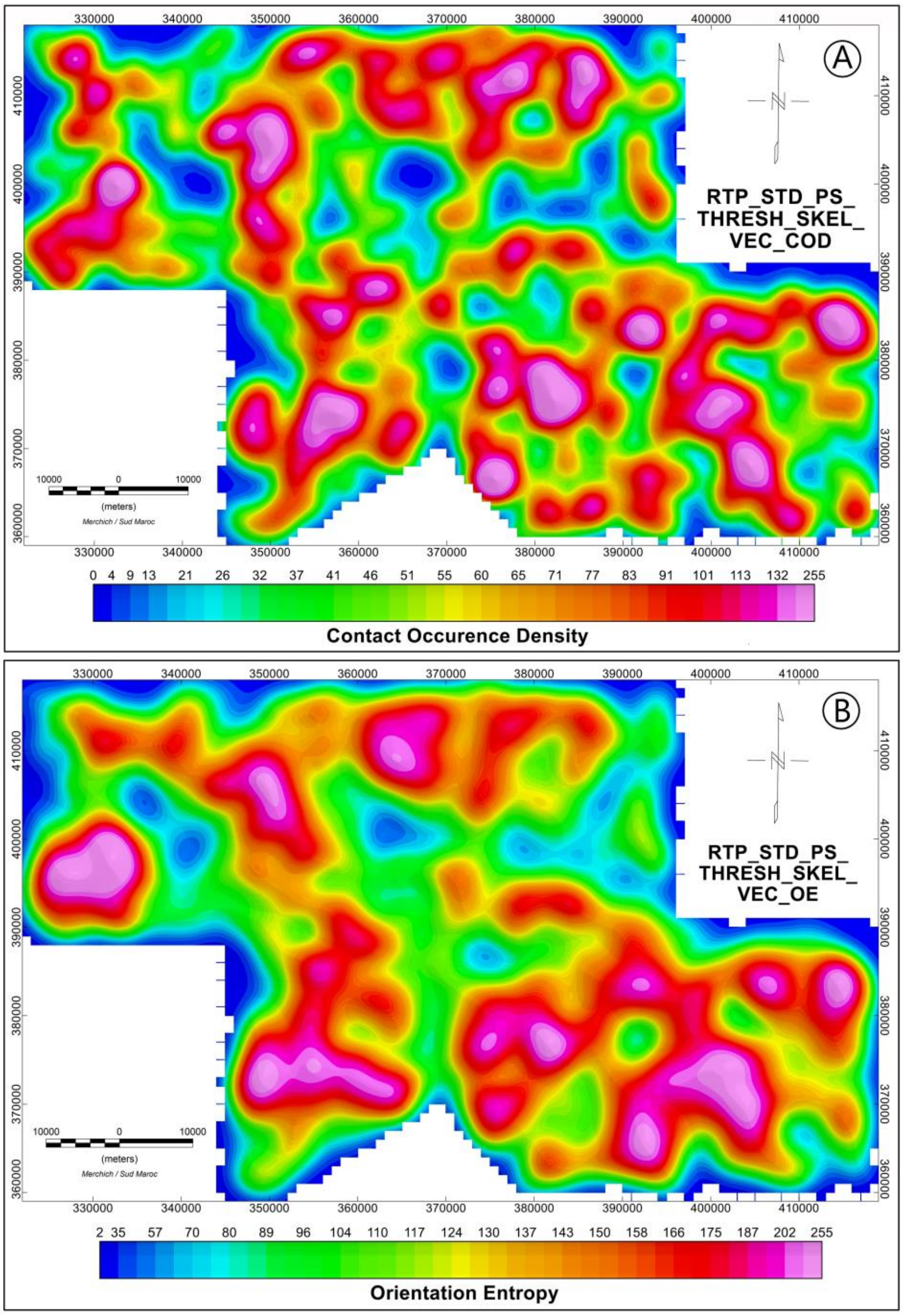

Figure 14. (**A**) Contact occurrence density map (structural complexity). (**B**) Orientation entropy map.

3.5. Euler Deconvolution and Analytic Signal

The Euler deconvolution process [97] was applied on the magnetic data to locate the positions and corresponding depth estimates of magnetic anomalies [98]; we are interested in contact and discontinuities, otherwise, we processed the deconvolution with structural index of 0 to enhance the intended geological features. This depth estimation method is frequently used since it adopts no specific geologic model [99]. The map effectively presents the dispersal of deep and near-surface magnetic sources within the explored part (Figure 18). The results exhibited a range of depths between 92 and 1402 m that match closely with the results obtained by [3–5,13] and were confirmed by the analytic signal spectrum (Figure 17B). In the predominant blue color zone (with depths less than 1400 m) situated mainly at the inlier center and spread over some portions within the suggested prospective area, the Euler deconvolution solutions support and match perfectly with the obtained results from the CET Grid and Porphyry Analysis.

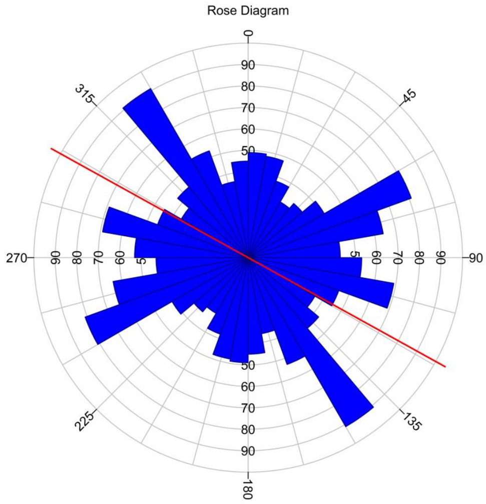

Figure 15. Rose diagram of the obtained results.

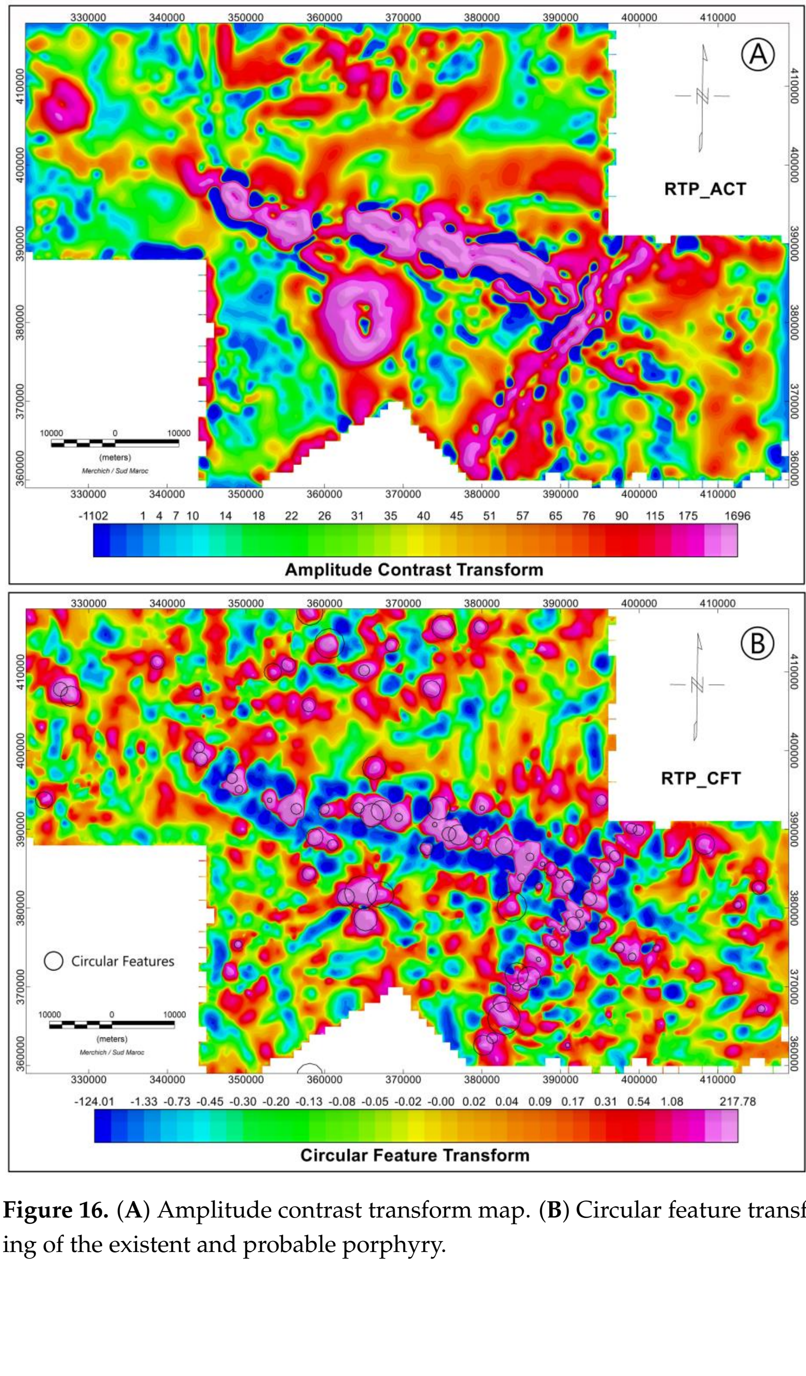

Figure 16. (**A**) Amplitude contrast transform map. (**B**) Circular feature transform map with contouring of the existent and probable porphyry.

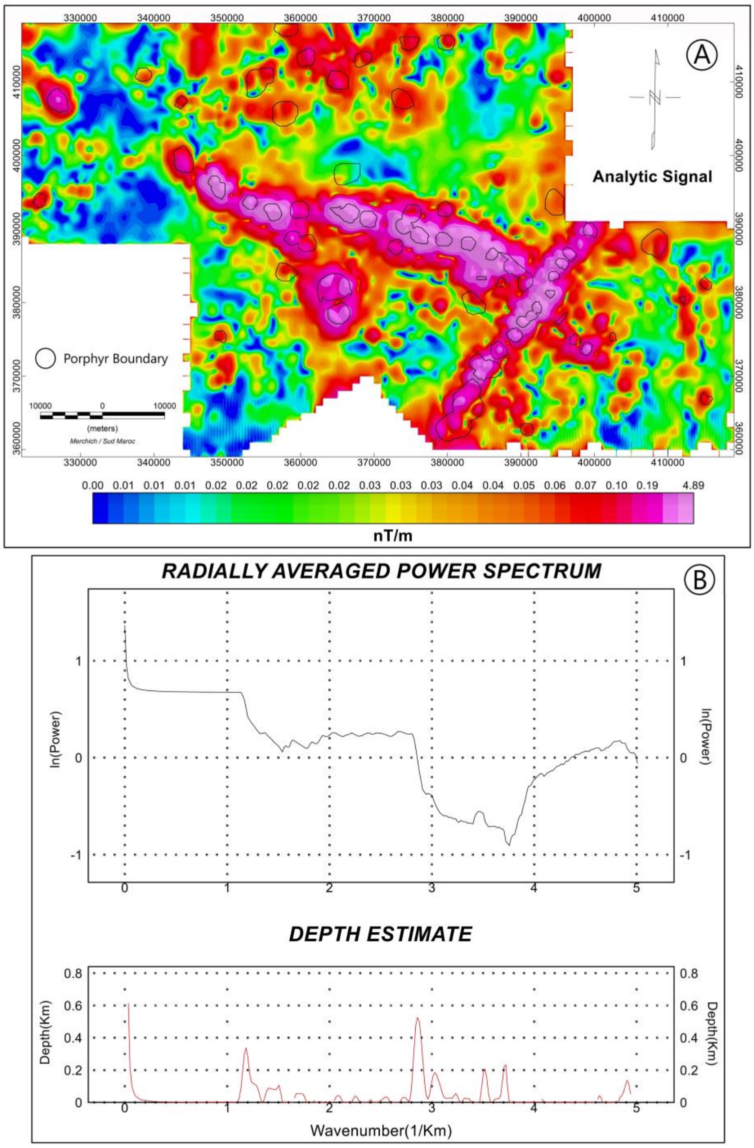

Figure 17. (**A**) Analytic signal map with contour boundaries of the existent and probable porphyry. (**B**) Depth estimation of magnetic sources by analytic signal spectrum.

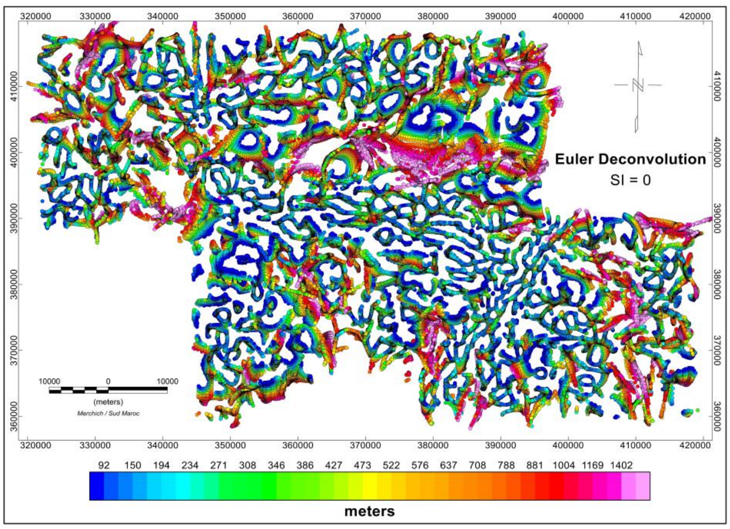

Figure 18. Euler deconvolution map for SI = 0.

4. Conclusions

The magnetic anomalies currently observed along the region reflect the different structure, composition, and geodynamic history of the Bou Azzer inlier and surrounding margins that developed during Precambrian and Phanerozoic time. Several magnetic domains with different magnetic patterns have been observed and provide new information about the spreading evolution and architecture of the inlier.

To illustrate this interpretation of the entire region, specifically the Bou Azzer inlier, the structural and mining potential map were also interpreted using CET Grid and Porphyry Analysis and other tools for magnetic modelling. The structural and mining potential field modelling of the area reveal that the region is favorable for cobalt and associated mineralizations regarding the observed structural complexity, mainly characterized by important discontinuities considered as potential zones for the circulation of hydrothermal fluids (zones of mineralization).

In addition, the obtained results already show different lateral heterogeneities in the area, indicating a complex tectonic event in addition to the thickness of the regional overburden. However, as only magnetic results exist along region through the Bou Azzer inlier, the interpretations of the susceptibilities of structures remain important, as magnetic structures are related to the regional geological context.

The geological and geophysical ground exploration is recommended and will be better integrated with the aeromagnetic survey at the scale of the studied region, essentially around and on the identified potential zones, to re-evaluate and update the tectonic evolution and kinematic and geodynamic context of the region in light of the new observations.

We also suggest to better link the region not covered by the aeromagnetic survey in the future. The segmentation of the Bou Azzer inlier is most likely controlled by the early rift and breakup history. Gravity and seismic investigation, as well as modelling and interpretations of the Bou Azzer inlier integrated with our observations, can be relevant to better assess the structure and evolution of the high-complexity zones.

More work is still required to fully constrain the evolution of the Bou Azzer inlier. A similar modern aeromagnetic survey on the uncovered regions will also be an obvious and relevant proposal to fully understand the spreading evolution of the extremity of the inlier. A remapping of the inlier will also be relevant to better understand the transition to the southern and northern spreading system initiated to the east and west of the inlier margins.

Author Contributions: Conceptualization, A.S., S.C., S.S., A.M. (Anselme Muzirafuti) and A.M. (Ahmed Manar); methodology, A.S., S.S., A.M. (Ahmed Manar) and A.M. (Anselme Muzirafuti); software, A.S., S.S., A.M. (Ahmed Manar) and A.M. (Abdelhalim Miftah); validation, A.S., S.C., S.S., A.M. (Ahmed Manar), Z.B., A.M. (Abdelhalim Miftah), M.A.Z., Y.Z., M.B. and A.M. (Anselme Muzirafuti); formal analysis, A.S., S.C., S.S. and A.M. (Anselme Muzirafuti); investigation, A.S.; resources, A.S. and A.M. (Anselme Muzirafuti); data curation, A.S.; writing—original draft preparation, A.S., S.C. and S.S.; writing—review and editing, A.S., S.C., S.S., A.M. (Ahmed Manar), Z.B., A.M. (Abdelhalim Miftah), M.A.Z., Y.Z., M.B. and A.M. (Anselme Muzirafuti); visualization, A.S., S.S., A.M. (Ahmed Manar), A.M. (Abdelhalim Miftah) and A.M. (Anselme Muzirafuti); supervision, S.C., S.S., A.M. (Ahmed Manar), A.M. (Anselme Muzirafuti) and Z.B.; project administration, A.S.; funding acquisition, A.S. and A.M. (Anselme Muzirafuti). All authors have read and agreed to the published version of the manuscript.

Funding: This research received no external funding.

Institutional Review Board Statement: Not applicable.

Informed Consent Statement: Not applicable.

Data Availability Statement: The data presented in this study are available on request from the corresponding authors.

Conflicts of Interest: The authors declare no conflict of interest.

References

1. Nathan, D.; Aitken, A.; Holden, E.J.; Wong, J. Imaging Sedimentary Basins from High-Resolution Aeromagnetics and Texture Analysis. *Comput. Geosci.* **2020**, *136*, 104396. [CrossRef]
2. Holden, E.J.; Dentith, M.; Kovesi, P. Towards the Automated Analysis of Regional Aeromagnetic Data to Identify Regions Prospective for Gold Deposits. *Comput. Geosci.* **2008**, *34*, 1505–1513. [CrossRef]
3. Miftah, A.; El Azzab, D.; Attou, A.; Manar, A. Contribution of the Geomagnetism to the Region of the Massif Jbel Saghro Geology, Eastern Anti-Atlas, Morocco. *Arab. J. Geosci.* **2017**, *10*, 460. [CrossRef]
4. Miftah, A.; El Azzab, D.; Attou, A.; Rachid, A.; Ouchchen, M.; Soulaimani, A.; Soulaimani, S.; Manar, A. Combined Analysis of Helicopter-Borne Magnetic and Stream Sediment Geochemical Data around an Ancient Tiouit Gold Mine (Eastern Anti-Atlas, Morocco): Geological and Mining Interpretations. *J. Afr. Earth Sci.* **2021**, *175*, 104093. [CrossRef]
5. Bouougri, E.H.; Saquaque, A. Lithostratigraphic Framework and Correlation of the Neoproterozoic Northern West African Craton Passive Margin Sequence (Siroua-Zenaga-Bouazzer Elgraara Inliers, Central Anti-Atlas, Morocco): An Integrated Approach. *J. Afr. Earth Sci.* **2004**, *39*, 227–238. [CrossRef]
6. Álvaro, J.J.; Pouclet, A.; Ezzouhairi, H.; Soulaimani, A.; Bouougri, E.H.; Imaz, A.G.; Fekkak, A. Early Neoproterozoic Rift-Related Magmatism in the Anti-Atlas Margin of the West African Craton, Morocco. *Precambrian Res.* **2014**, *255*, 433–442. [CrossRef]
7. Aabi, A.; Hejja, Y.; Bba, A.N.; Baidder, L.; Fekkak, A.; Bannari, A.; Maacha, L. Polyphase Tectonics, Fault Kinematics and Metallogenic Implications at the Fringe of a Craton (Anti-Atlas, Morocco). *J. Afr. Earth Sci.* **2022**, *196*, 104731. [CrossRef]
8. Vasuki, Y.; Holden, E.J.; Kovesi, P.; Micklethwaite, S. Semi-Automatic Mapping of Geological Structures Using UAV-Based Photogrammetric Data: An Image Analysis Approach. *Comput. Geosci.* **2014**, *69*, 22–32. [CrossRef]
9. Kovesi, P.; Holden, E.J.; Wong, J. Interactive Multi-Image Blending for Visualization and Interpretation. *Comput. Geosci.* **2014**, *72*, 147–155. [CrossRef]
10. Holden, E.-J.; Fu, S.C.; Kovesi, P.; Dentith, M.; Bourne, B.; Hope, M. Automatic Identification of Responses from Porphyry Intrusive Systems within Magnetic Data Using Image Analysis. *J. Appl. Geophys.* **2011**, *74*, 255–262. [CrossRef]
11. Soulaimani, S.; Chakiri, S.; Manar, A.; Soulaimani, A.; Miftah, A.; Bouiflane, M. Potential-Field Geophysical Data Inversion for 3D Modelling and Reserve Estimation (Example of the Hajjarmine, Guemassamassif, Morocco): Magnetic and Gravity Data Case. *C. R. Geosci.* **2020**, *352*, 139–155. [CrossRef]
12. Soulaimani, S.; Chakiri, S.; Manar, A.; Soulaimani, A.; Miftah, A.; Boujamaoui, M. Gravity and Magnetic Data Processing Further Constrained Inversion for 3D Modelling and Tonnage Calculation. *Appl. Earth Sci. Trans. Inst. Min. Metall.* **2020**, *129*, 133–146. [CrossRef]
13. Bouiflane, M.; Manar, A.; Medina, F.; Youbi, N.; Rimi, A. Mapping and Characterization from Aeromagnetic Data of the Foum Zguid Dolerite Dyke (Anti-Atlas, Morocco) a Member of the Central Atlantic Magmatic Province (CAMP). *Tectonophysics* **2017**, *708*, 15–27. [CrossRef]
14. Mamouch, Y.; Attou, A.; Miftah, A.; Ouchchen, M.; Dadi, B.; Achkouch, L.; Et-Tayea, Y.; Allaoui, A.; Boualoul, M.; Randazzo, G.; et al. Mapping of Hydrothermal Alteration Zones in the Kelâat M'Gouna Region Using Airborne Gamma-Ray Spectrometry and Remote Sensing Data: Mining Implications (Eastern Anti-Atlas, Morocco). *Appl. Sci.* **2022**, *12*, 957. [CrossRef]
15. Holden, E.J.; Wong, J.C.; Wedge, D.; Martis, M.; Lindsay, M.; Gessner, K. Improving Assessment of Geological Structure Interpretation of Magnetic Data: An Advanced Data Analytics Approach. *Comput. Geosci.* **2016**, *87*, 101–111. [CrossRef]
16. Vasuki, Y.; Holden, E.J.; Kovesi, P.; Micklethwaite, S. An Interactive Image Segmentation Method for Lithological Boundary Detection: A Rapid Mapping Tool for Geologists. *Comput. Geosci.* **2017**, *100*, 27–40. [CrossRef]
17. Holden, E.J.; Kovesi, P.; Dentith, M.C.; Wedge, D.; Wong, J.C.; Fu, S.C. Detection of Regions of Structural Complexity within Aeromagnetic Data Using Image Analysis. In Proceedings of the 25th International Conference Image and Vision Computing New Zealand, Queenstown, New Zealand, 8–9 November 2010; pp. 1–8.
18. Malusà, M.G.; Polino, R.; Feroni, A.C.; Ellero, A.; Ottria, G.; Baidder, L.; Musumeci, G. Post-Variscan Tectonics in Eastern Anti-Atlas (Morocco). *Terra Nov.* **2007**, *19*, 481–489. [CrossRef]
19. Missenard, Y. Le Relief Des Atlas Marocains: Contribution Des Processus Asthénosphériques et Du Raccourcissement Crustal, Aspects Chronologiques. Ph.D. Thesis, Université de Cergy Pontoise, Cergy, France, 2007.
20. Soulaimani, A.; Ouanaimi, H.; Saddiqi, O.; Baidder, L.; Michard, A. The Anti-Atlas Pan-African Belt (Morocco): Overview and Pending Questions. *C. R. Geosci.* **2018**, *350*, 279–288. [CrossRef]
21. Tourneur, E.; Chauvet, A.; Kouzmanov, K.; Tuduri, J.; Paquez, C.; Sizaret, S.; Karfal, A.; Moundi, Y.; El Hassani, A. Co-Ni-Arsenide Mineralisation in the Bou Azzer District (Anti-Atlas, Morocco): Genetic Model and Tectonic Implications. *Ore Geol. Rev.* **2021**, *134*, 104128. [CrossRef]
22. Hefferan, K.P.; Admou, H.; Karson, J.A.; Saquaque, A. Anti-Atlas (Morocco) Role in Neoproterozoic Western Gondwana Reconstruction. *Precambrian Res.* **2000**, *103*, 89–96. [CrossRef]
23. Berrahma, M.; Delaloye, M. Données Géochronologiques Nouvelles Sur Le Massif Volcanique Du Siroua (Anti-Atlas, Maroc). *J. Afr. Earth Sci.* **1989**, *9*, 651–656. [CrossRef]
24. Naidoo, D.D.; Bloomer, S.H.; Saquaque, A.; Hefferan, K. Geochemistry and Significance of Metavolcanic Rocks from the Bou Azzer-El Graara Ophiolite (Morocco)—Reply. *Precambrian Res.* **1993**, *62*, 369–371. [CrossRef]
25. Bodinier, J.L.; Dupuy, C.; Dostal, J. Geochemistry of Precambrian Ophiolites from Bou Azzer, Morocco. *Contrib. Mineral. Petrol.* **1984**, *87*, 43–50. [CrossRef]

26. Blein, O.; Razin, P.; Chevremont, P.; Baudin, T.; Gasquet, D.; Abderrahmane, S.; Admou, H.; Youbi, N.; Bouabdelli, M.; Anzar, C. Notice Explicative Carte Géologie Maroc (1/50,000), Feuille d'Alougoum. *Notes Mémoires Serv. Géologique Maroc* **2011**, *534*, halsde-00950540.
27. Leblanc, M.; Billaud, P. A Volcano-Sedimentary Copper Deposit on a Continental Margin of Upper Proterozoic Age; Bleida (Anti-Atlas, Morocco). *Econ. Geol.* **1978**, *73*, 1101–1111. [CrossRef]
28. Leblanc, M.; Lancelot, J.R. Geodynamic Interpretation of the Pan-African Domain (Late Precambrian) of the Anti-Atlas, Morocco, from Geology and Geochronology. *Can. J. Earth Sci.* **1980**, *17*, 142–155. [CrossRef]
29. Leblanc, M.; Billard, P. Cobalt Arsenide Orebodies Related to an Upper Proterozoic Ophiolite: Bou Azzer (Morocco). *Econ. Geol.* **1982**, *77*, 162–175. [CrossRef]
30. Hefferan, K.; Soulaimani, A.; Samson, S.D.; Admou, H.; Inglis, J.; Saquaque, A.; Latifa, C.; Heywood, N. A Reconsideration of Pan African Orogenic Cycle in the Anti-Atlas Mountains, Morocco. *J. Afr. Earth Sci.* **2014**, *98*, 34–46. [CrossRef]
31. El Hadi, H.; Simancas, J.F.; Martínez-Poyatos, D.; Azor, A.; Tahiri, A.; Montero, P.; Fanning, C.M.; Bea, F.; González-Lodeiro, F. Structural and Geochronological Constraints on the Evolution of the Bou Azzer Neoproterozoic Ophiolite (Anti-Atlas, Morocco). *Precambrian Res.* **2010**, *182*, 1–14. [CrossRef]
32. Gahlan, H.A.; Arai, S.; Ahmed, A.H.; Ishida, Y.; Abdel-Aziz, Y.M.; Rahimi, A. Origin of Magnetite Veins in Serpentinite from the Late Proterozoic Bou-Azzer Ophiolite, Anti-Atlas, Morocco: An Implication for Mobility of Iron during Serpentinization. *J. Afr. Earth Sci.* **2006**, *46*, 318–330. [CrossRef]
33. Hodel, F.; Macouin, M.; Triantafyllou, A.; Carlut, J.; Berger, J.; Rousse, S.; Ennih, N.; Trindade, R.I.F. Unusual Massive Magnetite Veins and Highly Altered Cr-Spinels as Relics of a Cl-Rich Acidic Hydrothermal Event in Neoproterozoic Serpentinites (Bou Azzer Ophiolite, Anti-Atlas, Morocco). *Precambrian Res.* **2017**, *300*, 151–167. [CrossRef]
34. Subías, I.; Fanlo, I.; Hajjar, Z.; Gervilla, F.; Billström, K. Isotopic Constraints on the Age and Source of Ore-Forming Fluids of the Bou Azzer Arsenide Ores (Morocco). *Ore Geol. Rev.* **2022**, *143*, 104769. [CrossRef]
35. Maacha, L.; Alansari, A.; Saquaque, A.; Soulaimani, A. The Bou Azzer Cobalt-Nickel-Arsenic District. *Les Mines L'Anti-Atlas Cent.* **2012**, *9*, 91–97.
36. Gervilla, F.; Padrón-Navarta, J.A.; Kerestedjian, T.; Sergeeva, I.; González-Jiménez, J.M.; Fanlo, I. Formation of Ferrian Chromite in Podiform Chromitites from the Golyamo Kamenyane Serpentinite, Eastern Rhodopes, SE Bulgaria: A Two-Stage Process. *Contrib. Mineral. Petrol.* **2012**, *164*, 643–657. [CrossRef]
37. Ahmed, A.H.; Arai, S.; Ikenne, M. Mineralogy and Paragenesis of the Co-Ni Arsenide Ores of Bou Azzer, Anti-Atlas, Morocco. *Econ. Geol.* **2009**, *104*, 249–266. [CrossRef]
38. Vinet, L.; Zhedanov, A. A "missing" Family of Classical Orthogonal Polynomials. *J. Phys. A Math. Theor.* **2011**, *44*, 085201. [CrossRef]
39. Ennaciri, A.; Barbanson, L.; Touray, J.C. Mineralized Hydrothermal Solution Cavities in the Co-As Aït Ahmane Mine (Bou Azzer, Morocco). *Miner. Depos.* **1995**, *30*, 75–77. [CrossRef]
40. Levresse, G. Contribution à l'établissement d'un Modèle Génétique Des Gisements d'Imiter (Ag-Hg), Bou Madine (Pb-Zn-Cu-Ag-Au) et Bou Azzer (Co-Ni-As-Au-Ag) Dans l'An Ti-Atlas Marocain. Ph.D. Thesis, Institut National Polytechnique de Lorraine, Vandœuvre-lès-Nancy, France, 2001.
41. Gervilla, F.; Fanlo, I.; Colás, V.; Subías, I. Mineral Compositions and Phase Relations of Ni-Co-Fe Arsenide Ores from the Aghbar Mine, Bou Azzer, Morocco. *Can. Mineral.* **2012**, *50*, 447–470. [CrossRef]
42. Maacha, L.; Azizi-Samir, M.R.; Bouchta, R. Gisements Cobaltifères Du District de Bou Azzer (Anti-Atlas): Structure et Conditions de Génèse. *Chron. Rech. Minière* **1998**, *531/532*, 65–75.
43. Maacha, L. Etude Géologique et Métallogénique Des Gisements Cobaltifères de Bou Azzer-Centre (Anti-Atlas, Maroc). Ph. D. Thesis, Mém. CEA University, Marrakech, Morocco, 1994; p. 119.
44. Maacha, L. Gisement Cobaltifère de Bou Azzer (Anti-Atlas): Structures, Minéralogie et Conditions de Genèse. *Chron. Rech. Minière* **1996**, *531–532*, 65–75.
45. Maacha, L.; Ennaciri, O.; Ghorfi, M.E.L.; Saquaque, A.; Alansari, A.; Soulaimani, A. 2.4-Le District à Cobalt, Nickel et Arsenic de Bou Azzer (Anti-Atlas Central). *Les Mines L'Anti-Atlas Cent.* **1971**, *9*, 91–97.
46. Ghorfi, M.; Oberthür, T.; Melcher, F.; Lüders, V.; El Boukhari, A.; Maacha, L.; Ziadi, R.; Baoutoul, H. Gold-Palladium Mineralization at Bleïda Far West, Bou Azzer-El Graara Inlier, Anti-Atlas, Morocco. *Miner. Depos.* **2006**, *41*, 549–564. [CrossRef]
47. Ikenne, M.; Souhassou, M.; Saintilan, N.J.; Karfal, A.; Hassani, A.E.L.; Moundi, Y.; Ousbih, M.; Ezzghoudi, M.; Zouhir, M.; Maacha, L. Cobalt–Nickel–Copper Arsenide, Sulfarsenide and Sulfide Mineralization in the Bou Azzer Window, Anti-Atlas, Morocco: One Century of Multi-Disciplinary and Geological Investigations, Mineral Exploration and Mining. *Geol. Soc. Lond. Spec. Publ.* **2021**, *502*, 45–66. [CrossRef]
48. Bouabdellah, M.; Maacha, L.; Levresse, G.; Saddiqi, O. The Bou Azzer Co–Ni–Fe–As(±Au ± Ag) District of Central Anti-Atlas (Morocco): A Long-Lived Late Hercynian to Triassic Magmatic-Hydrothermal to Low-Sulphidation Epithermal System. In *Mineral Deposits of North Africa*; Springer: Cham, Switzerland, 2016; pp. 229–247.
49. Walsh, G.J.; Benziane, F.; Aleinikoff, J.N.; Harrison, R.W.; Yazidi, A.; Burton, W.C.; Quick, J.E.; Saadane, A. Neoproterozoic Tectonic Evolution of the Jebel Saghro and Bou Azzer-El Graara Inliers, Eastern and Central Anti-Atlas, Morocco. *Precambrian Res.* **2012**, *216–219*, 23–62. [CrossRef]

50. Clauer, N. *Géochimie Isotopique Du Strontium Des Milieux Sédimentaires. Application à La Géochronologie de La Couverture Du Craton Ouest-Africain*; Persée-Portail des Revues Scientifiques en SHS: Lyon, France, 1976; Volume 45.
51. Inglis, J.D.; MacLean, J.S.; Samson, S.D.; D'Lemos, R.S.; Admou, H.; Hefferan, K. A Precise U-Pb Zircon Age for the Bleïda Granodiorite, Anti-Atlas, Morocco: Implications for the Timing of Deformation and Terrane Assembly in the Eastern Anti-Atlas. *J. Afr. Earth Sci.* **2004**, *39*, 277–283. [CrossRef]
52. Billaud, P. Les Structures Tectoniques Pan Africaines Du Gisement de Cuivre de Bleida. Ph.D. Thesis, Université des Sciences et Techniques du Languedoc, Montpellier, France, 1977.
53. Maacha, L.; Elghorfi, M.; Zouhair, M.; Sadiqui; Soulaimani, A. Minéralisations Sulfurées de Cuivre de La Série de Plateforme de Bleïda Boutonnière de Bou Azzer-El Grâara (Anti-Atlas Occidental). *Notes Mem. Serv. Geol.* **2013**, *579*, 1–7.
54. Mouttaqi, A.; Sagon, J.-P. Le Gisement de Cuivre de Bleida '(Anti-Atlas Central): Une Interférence Entre Les Processus de Remplacement et d'exhalaison Dans Un Contexte de Rift. *Chron. Rech. Manière* **1999**, *536–537*, 5–21.
55. El Azzab, D.; Ghfir, Y.; Miftah, A. Geological Interpretation of the Rifian Foreland Gravity Anomalies and 3D Modeling of Their Hercynian Granites (Northeastern Morocco). *J. Afr. Earth Sci.* **2019**, *150*, 584–594. [CrossRef]
56. Anderson, E.D.; Dentith, M.; Stephen, T. Mudge: Geophysics for the Mineral Exploration Geoscientist. *Miner. Depos.* **2015**, *50*, 139–140. [CrossRef]
57. Ouchchen, M.; Boutaleb, S.; Abia, E.H.; El Azzab, D.; Abioui, M.; Mickus, K.L.; Miftah, A.; Echogdali, F.Z.; Dadi, B. Structural Interpretation of the Igherm Region (Western Anti Atlas, Morocco) from an Aeromagnetic Analysis: Implications for Copper Exploration. *J. Afr. Earth Sci.* **2021**, *176*, 104140. [CrossRef]
58. Ravat, D. Reduction to Pole. In *Encyclopedia of Geomagnetism and Paleomagnetism*; Gubbins, D., Herrero-Bervera, E., Eds.; Springer: Dordrecht, The Netherlands, 2007; pp. 856–858, ISBN 978-1-4020-4423-6.
59. Bba, A.N.; Boujamaoui, M.; Amiri, A.; Hejja, Y.; Rezouki, I.; Baidder, L.; Inoubli, M.H.; Manar, A.; Jabour, H. Structural Modeling of the Hidden Parts of a Paleozoic Belt: Insights from Gravity and Aeromagnetic Data (Tadla Basin and Phosphates Plateau, Morocco). *J. Afr. Earth Sci.* **2019**, *151*, 506–522. [CrossRef]
60. Baranov, V. A New Method for Interpretation of Aeromagnetic Maps: Pseudo-Gravimetric Anomalies. *Geophysics* **1957**, *22*, 359–382. [CrossRef]
61. Baranov, V.; Naudy, H. Numerical Calculation of the Formula of Reduction to the Magnetic Pole. *Geophysics* **1964**, *29*, 67–79. [CrossRef]
62. Grant, F.S. Review of Data Processing and Interpretation Methods in Gravity and Magnetics, 1964–1971. *Geophysics* **1972**, *37*, 647–661. [CrossRef]
63. O'Connell, M.D.; Smith, R.S.; Vallee, M.A. Gridding Aeromagnetic Data Using Longitudinal and Transverse Horizontal Gradients with the Minimum Curvature Operator. *Lead. Edge* **2005**, *24*, 142–145. [CrossRef]
64. Osinowo, O.O.; Alumona, K.; Olayinka, A.I. Analyses of High Resolution Aeromagnetic Data for Structural and Porphyry Mineral Deposit Mapping of the Nigerian Younger Granite Ring Complexes, North-Central Nigeria. *J. Afr. Earth Sci.* **2020**, *162*, 103705. [CrossRef]
65. Osinowo, O.O.; Abdulmumin, Y. Basement Configuration and Lineaments Mapping from Aeromagnetic Data of Gongola Arm of Upper Benue Trough, Northeastern Nigeria. *J. Afr. Earth Sci.* **2019**, *160*, 103597. [CrossRef]
66. Ekwok, S.E.; Akpan, A.E.; Kudamnya, E.A. Exploratory Mapping of Structures Controlling Mineralization in Southeast Nigeria Using High Resolution Airborne Magnetic Data. *J. Afr. Earth Sci.* **2020**, *162*, 103700. [CrossRef]
67. Forson, E.D.; Wemegah, D.D.; Hagan, G.B.; Appiah, D.; Addo-Wuver, F.; Adjovu, I.; Otchere, F.O.; Mateso, S.; Menyeh, A.; Amponsah, T. Data-Driven Multi-Index Overlay Gold Prospectivity Mapping Using Geophysical and Remote Sensing Datasets. *J. Afr. Earth Sci.* **2022**, *190*, 104504. [CrossRef]
68. Kovesi, P. Image Features from Phase Congruency. *Videre* **1999**, *1*, C3.
69. Lee, T.D. Symmetry and Asymmetry. *Proc. Nucl. Phys. A* **2008**, *805*, 54c–71c. [CrossRef]
70. Kovesi, P. Symmetry and Asymmetry from Local Phase. In Proceedings of the 1997 Tenth Australian Joint Conference on Artifical Intelligence, Perth, Australia, 30 November–4 December 1997; pp. 185–190.
71. Eldosouky, A.M.; Abdelkareem, M.; Elkhateeb, S.O. Integration of Remote Sensing and Aeromagnetic Data for Mapping Structural Features and Hydrothermal Alteration Zones in Wadi Allaqi Area, South Eastern Desert of Egypt. *J. Afr. Earth Sci.* **2017**, *130*, 28–37. [CrossRef]
72. Lam, L.; Lee, S.W. Thinning Methodologies—A Comprehensive Survey. *IEEE Trans. Pattern Anal. Mach. Intell.* **1992**, *14*, 869–885. [CrossRef]
73. Assran, A.S.M.; El Qassas, R.A.Y.; Yousef, M.H.M. Detection of Prospective Areas for Mineralization Deposits Using Image Analysis Technique of Aeromagnetic Data around Marsa Alam-Idfu Road, Eastern Desert, Egypt. *Egypt. J. Pet.* **2019**, *28*, 61–69. [CrossRef]
74. Loy, G.; Zelinsky, A. Fast Radial Symmetry for Detecting Points of Interest. *IEEE Trans. Pattern Anal. Mach. Intell.* **2003**, *25*, 959–973. [CrossRef]
75. Pham, L.T.; Oksum, E.; Gómez-Ortiz, D.; Do, T.D. MagB_inv: A High Performance Matlab Program for Estimating the Magnetic Basement Relief by Inverting Magnetic Anomalies. *Comput. Geosci.* **2020**, *134*, 104347. [CrossRef]
76. Williams, D.J.; Shah, M. A Fast Algorithm for Active Contours and Curvature Estimation. *CVGIP Image Underst.* **1992**, *55*, 14–26. [CrossRef]

77. Thompson, D.T. EULDPH: A New Technique for Making Computer-Assisted Depth Estimates from Magnetic Data. *Geophysics* **1982**, *47*, 31–37. [CrossRef]
78. Reid, A.B.; Allsop, J.M.; Granser, H.; Millett, A.J.; Somerton, I.W. Magnetic Interpretation in Three Dimensions Using Euler Deconvolution. *Geophysics* **1990**, *55*, 80–91. [CrossRef]
79. Marson, I.; Klingele, E.E. Advantages of Using the Vertical Gradient of Gravity for 3-D Interpretation. *Geophysics* **1993**, *58*, 1588–1595. [CrossRef]
80. Stavrev, P.Y. Euler Deconvolution Using Differential Similarity Transformations of Gravity or Magnetic Anomalies. *Geophys. Prospect.* **1997**, *45*, 207–246. [CrossRef]
81. Mushayandebvu, M.F.; Van Driel, P.; Reid, A.B.; Fairhead, J.D. Magnetic Source Parameters of Two-Dimensional Structures Using Extended Euler Deconvolution. *Geophysics* **2001**, *66*, 814–823. [CrossRef]
82. Agarwal, B.N.P.; Srivastava, S. Analyses of Self-Potential Anomalies by Conventional and Extended Euler Deconvolution Techniques. *Comput. Geosci.* **2009**, *35*, 2231–2238. [CrossRef]
83. Nabighian, M.N. The Analytic Signal of Two-Dimensional Magnetic Bodies with Polygonal Cross-Section: Its Properties and Use for Automated Anomaly Interpretation. *Geophysics* **1972**, *37*, 507–517. [CrossRef]
84. Nabighian, M.N. Additional Comments on the Analytic Signal of Two-Dimensional Magnetic Bodies With Polygonal Cross-Section. *Geophysics* **1974**, *39*, 85–92. [CrossRef]
85. Nabighian, M.N. Toward a Three-Dimensional Automatic Interpretation of Potential Field Data via Generalized Hilbert Transforms: Fundamental Relations. *Geophysics* **1984**, *49*, 780–786. [CrossRef]
86. Roest, W.R.; Verhoef, J.; Pilkington, M. Magnetic Interpretation Using the 3-D Analytic Signal. *Geophysics* **1992**, *57*, 116–125. [CrossRef]
87. El-Khanchaoui, T.; Lahmam, M.; El-Boukhari, A.; El-Beraaouz, H. Neoproterozoic Granitoids from Khzama, Central Anti-Atlas, Morocco: Evolution Markers from Arc Magmatism to Alkaline Magmatism. *J. Afr. Earth Sci.* **2001**, *32*, 655–676. [CrossRef]
88. Nshimiyimana, F.; Essarraj, S.; Hibti, M.; Boulvais, P.; Boyce, A.J.; Marignac, C.; Maacha, L. The Koudia El Hamra Ag–Pb–Zn Deposit, Jebilet, Morocco: Mineralogy and Ore Fluid Characterization. *J. Afr. Earth Sci.* **2018**, *145*, 1–17. [CrossRef]
89. El Basbas, A.; Aissa, M.; Ouguir, H.; Mahdoudi, M.L.; Madi, A.; Zouhair, M. Ouansimi Copper Mineralization (Western Anti-Atlas, Morocco): Paragenetic Sequence and Circulation of Gangue Hosted Paleofluids. *J. Afr. Earth Sci.* **2020**, *162*, 103692. [CrossRef]
90. Ikenne, M.; Söderlund, U.; Ernst, R.E.; Pin, C.; Youbi, N.; El Aouli, E.H.; Hafid, A. A c. 1710 Ma Mafic Sill Emplaced into a Quartzite and Calcareous Series from Ighrem, Anti-Atlas–Morocco: Evidence That the Taghdout Passive Margin Sedimentary Group Is Nearly 1 Ga Older than Previously Thought. *J. Afr. Earth Sci.* **2017**, *127*, 62–76. [CrossRef]
91. El Janati, M. Application of Remotely Sensed ASTER Data in Detecting Alteration Hosting Cu, Ag and Au Bearing Mineralized Zones in Taghdout Area, Central Anti-Atlas of Morocco. *J. Afr. Earth Sci.* **2019**, *151*, 95–106. [CrossRef]
92. Anudu, G.K.; Stephenson, R.A.; Macdonald, D.I.M. Using High-Resolution Aeromagnetic Data to Recognise and Map Intra-Sedimentary Volcanic Rocks and Geological Structures across the Cretaceous Middle Benue Trough, Nigeria. *J. Afr. Earth Sci.* **2014**, *99*, 625–636. [CrossRef]
93. Mohammadpour, M.; Bahroudi, A.; Abedi, M. Three Dimensional Mineral Prospectivity Modeling by Evidential Belief Functions, a Case Study from Kahang Porphyry Cu Deposit. *J. Afr. Earth Sci.* **2021**, *174*, 104098. [CrossRef]
94. Jessell, M.; Santoul, J.; Baratoux, L.; Youbi, N.; Ernst, R.E.; Metelka, V.; Miller, J.; Perrouty, S. An Updated Map of West African Mafic Dykes. *J. Afr. Earth Sci.* **2015**, *112*, 440–450. [CrossRef]
95. Hejja, Y.; Baidder, L.; Ibouh, H.; Bba, A.N.; Soulaimani, A.; Gaouzi, A.; Maacha, L. Fractures Distribution and Basement-Cover Interaction in a Polytectonic Domain: A Case Study from the Saghro Massif (Eastern Anti-Atlas, Morocco). *J. Afr. Earth Sci.* **2020**, *162*, 103694. [CrossRef]
96. Bouougri, E.H. The Moroccan Anti-Atlas: The West African Craton Passive Margin with Limited Pan-African Activity. Implications for the Northern Limit of the Craton. *Precambrian Res.* **2003**, *120*, 179–183. [CrossRef]
97. Osagie, A.U.; Eshanibli, A.; Adepelumi, A.A. Structural Trends and Basement Depths across Nigeria from Analysis of Aeromagnetic Data. *J. Afr. Earth Sci.* **2021**, *178*, 104184. [CrossRef]
98. Akinlalu, A.A.; Adelusi, A.O.; Olayanju, G.M.; Adiat, K.A.N.; Omosuyi, G.O.; Anifowose, A.Y.B.; Akeredolu, B.E. Aeromagnetic Mapping of Basement Structures and Mineralisation Characterisation of Ilesa Schist Belt, Southwestern Nigeria. *J. Afr. Earth Sci.* **2018**, *138*, 383–391. [CrossRef]
99. Eldosouky, A.M.; Elkhateeb, S.O. Texture Analysis of Aeromagnetic Data for Enhancing Geologic Features Using Co-Occurrence Matrices in Elallaqi Area, South Eastern Desert of Egypt. *NRIAG J. Astron. Geophys.* **2018**, *7*, 155–161. [CrossRef]